Frustration relief and reorientation transition in the kagomelike dolerophanite

Amelia Panther, Alexander A. Tsirlin, Ioannis Rousochatzakis

Frustration relief and reorientation transition in the kagomelike dolerophanite Cu₂OSO₄

Amelia Panther [○],[1,*] Alexander A. Tsirlin [○],[2,3] and Ioannis Rousochatzakis [○][1]

[1]*Department of Physics, Loughborough University, Loughborough LE11 3TU, United Kingdom*
[2]*Experimental Physics VI, Center for Electronic Correlations and Magnetism, University of Augsburg, 86159 Augsburg, Germany*
[3]*Felix Bloch Institute for Solid-State Physics, Leipzig University, 04103 Leipzig, Germany*

We present a theoretical study of dolerophanite Cu₂OSO₄, a layered kagomelike spin-$\frac{1}{2}$ magnetic insulator that can be described either as a system of chains coupled through dimers or as a kagome lattice where every third spin is replaced by a ferromagnetic spin dimer. Building on insights from *ab initio* calculations, classical numerical minimizations, and semiclassical expansions, we arrive at a minimal microscopic description that accounts for the experimental data reported so far, including the nature of the magnetic order, the reported spin length, and the observed anisotropy. The latter arises by a peculiar competition between the antisymmetric (Dzyaloshinskii-Moriya) and the symmetric part of the exchange anisotropy, which gives rise to a two-step reorientation process involving two successive continuous phase transitions. In this paper, we uncover mechanisms stabilizing canted ferrimagnetic order in kagome systems and highlight strong magnetic anisotropy in the presence of dissimilar magnetic orbitals on crystallographically nonequivalent Cu sites. We also show how these anisotropy terms affect the spin-wave spectrum and how they can be tracked experimentally.

I. INTRODUCTION

The search for quantum spin liquids has remained at the forefront of condensed matter and quantum magnetism research for many decades [1–9] since Anderson's proposal of the resonating valence bond idea [10–13]. One of the main classes of candidate materials that has been explored intensively over the years is the transition-metal compounds with dominant isotropic interactions and strong geometric frustration, most notably the three-dimensional (3D) pyrochlores and quasi-two-dimensional (quasi-2D) kagome magnets [1,2,14,15]. In such materials, spins can evade magnetic ordering down to very low temperatures, despite their strong exchange interactions, due to the proliferation of infinite competing states at low energy scales. In conjunction with low dimensionality and low spin quantum number S, this competition magnifies the effects of quantum-mechanical fluctuations and opens the possibility for unconventional classical and nonclassical states, including spin nematics, valence bond crystals, and gapped and gapless spin liquids [1–4,6–9].

While the above ingredients—frustration, low dimensionality, and low spin—are present in many of the candidate materials that have been identified and characterized over the years, the broader consensus is that these same ingredients are also responsible for the high sensitivity to perturbations that are inevitably present in these compounds, such as longer-range interactions, magnetic anisotropy, and various forms of randomness. Understanding the role of these perturbations is therefore crucial for explaining experimental data and for developing a useful phenomenology for the search of unconventional states.

Here, we present a theoretical study of dolerophanite Cu₂OSO₄, a highly frustrated, quasi-2D, kagomelike magnet, where magnetic anisotropy plays a key role. Cu₂OSO₄ has been known as a mineral since the early 1960s [16]. Its structural characterization has been presented in Refs. [17–19], but its magnetic behavior was explored only recently [20–22]. The geometry of a given layer in Cu₂OSO₄ can be thought of as a system of chains joined through dimers or, alternatively, as a kagome lattice where every third spin is replaced by a dimer (Fig. 1). The material consists of two symmetry-nonequivalent Cu²⁺ ions denoted as Cu1 and Cu2; the ions form the kagome lattice where every third vertex is occupied by a Cu2 dimer, and Cu1 ions form chains along the **b** axis. As it turns out, the two spin-$\frac{1}{2}$ moments that make up a given dimer are so strongly ferromagnetically (FM) coupled that it would also be possible to consider an effective mixed-spin kagome model where one-third of the sites is represented by $S = 1$ moments.

At first glance, experimental data for Cu₂OSO₄ suggest only a weak magnetic anisotropy revealed by the Curie-Weiss temperatures (Θ_{CW}) of -71, -75, and -70 K measured along the **a**, **b**, and **c*** directions, respectively [22]. While the negative Θ_{CW} values would suggest predominantly antiferromagnetic (AFM) couplings, the magnetic ground state of Cu₂OSO₄ determined by neutron diffraction below $T_N = 20$ K is best described as a canted ferrimagnet [22]. Spins adopt a uniform coplanar configuration with a 120°-like structure in
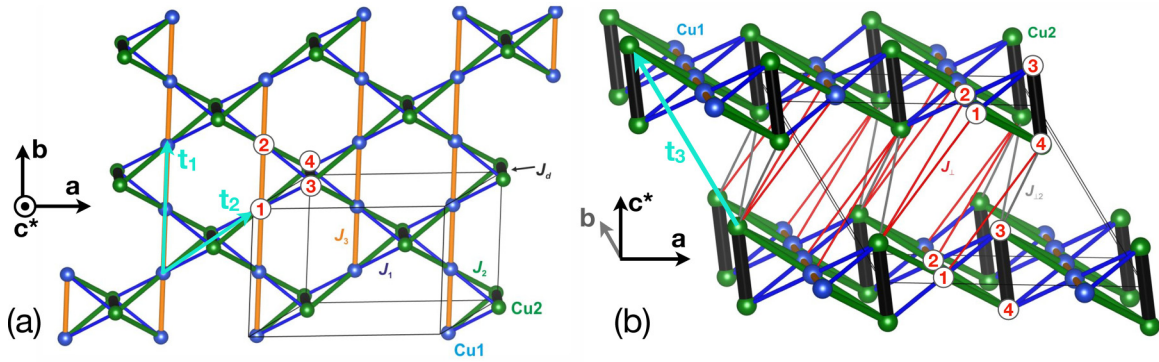
FIG. 1. (a) (a, b) view of a single layer of Cu_2OSO_4. Cu1 and Cu2 atoms are shown by blue and green spheres, respectively. The exchange coupling J_3 (orange) couples nearest-neighbor (NN) Cu1 atoms along chains on the **b** axis, J_d (thicker black lines) couples NN Cu2 atoms, and J_1 and J_2 couple neighboring Cu1 and Cu2 atoms (blue and green lines, respectively). The vectors $\mathbf{t}_1 = \mathbf{b}$, $\mathbf{t}_2 = (\mathbf{a} + \mathbf{b})/2$ and $\mathbf{t}_3 = \mathbf{c}$ are primitive translation vectors, and the numbers 1–4 (in red) label the four atoms of the basis. (b) Two layers of Cu_2OSO_4, showing the topology of the couplings $J_\perp$ and $J_{\perp 2}$ (red and gray lines, respectively)

the ab plane. The FM coupled Cu2 spins point along the **b** axis, resulting in an uncompensated total magnetic moment of $\sim 0.23(3)\,\mu_B$/Cu along this direction [21,22]. This value is remarkably close to the classical value of $\mu_B/4$ expected for the coplanar $120°$ spin arrangement in a mixed-spin kagome magnet. Moreover, the FM alignment of adjacent kagome layers implies that the total moments from different layers do not compensate each other.

Reflecting on these preliminary reports raises some important questions, which we seek to answer in this paper. First and foremost, we wish to construct a minimal microscopic model that accounts for the experimental data [20–22] and elucidate to what extent frustration of the kagome layers can account for the physics of Cu_2OSO_4. We also wish to examine the origin of the uncompensated magnetic moment and understand why it is pinned to a specific direction in the crystal structure and what determines the preferred plane for the coplanar spins.

Ultimately, in addressing these questions, we also aim to understand what sets Cu_2OSO_4 apart from the conventional kagome physics. At first glance, such a deviation is not unexpected due to the structural peculiarities of Cu_2OSO_4, particularly the presence of four Cu sites in the unit cell, instead of three, the absence of a threefold symmetry, and the inequivalence between the nearest-neighbor (NN) exchange paths. However, a closer analysis reveals that, despite these differences, the Heisenberg model of Cu_2OSO_4 remains highly frustrated, with an infinite ground-state manifold that is like that of the kagome francisites [23] and undistorted kagome magnets. However, the observation of a robust low-temperature ordered state with an almost classical value of the spin lengths [21,22] indicates minimal quantum fluctuations despite the frustration.

This brings us to the next main focus of this paper, which is to uncover the key role played by the magnetic anisotropy in this compound. As we show below, the lifting of the infinite ground-state degeneracy of the isotropic model and the selection of the observed, almost classical order arises from a nontrivial interplay of the antisymmetric part of the exchange anisotropy, i.e., the Dzyaloshinskii-Moriya (DM) interactions [24,25], and the symmetric (traceless) part, which we shall denote as **T** in this paper. According to our density functional

theory (DFT) calculations, the relevant DM vectors feature significant components along the crystallographic $\mathbf{c}^*$ axis and much weaker components in the ab plane. This hierarchy explains the selection of the observed uniform coplanar state and the pinning of the spins on the ab plane but fails to reproduce the direction of the uncompensated moment in that plane, as the in-plane DM components select the **a** and not the (observed) **b** axis. The inclusion of the symmetric part of the exchange anisotropy resolves this final puzzle and leads to a reorientation of the total moment along **b**, provided this anisotropy has large enough strength to override the effect of the in-plane DM components and it has the appropriate sign. Our DFT calculations for one of the most relevant bonds confirm explicitly that such an anisotropy is present in Cu_2OSO_4. We further show that the reorientation of the total moment proceeds via a two-step process involving an intermediate phase and that the spin gap depends very sensitively on the interplay between the in-plane DM components and the symmetric part of the exchange anisotropy.

Having identified the right minimal model, our final aim is to carry out self-consistent checks but also make predictions for further experiments which, in turn, will allow for more quantitative estimates of the microscopic coupling parameters in this complex, multisublattice system. To that end, we shall present a study of the response of Cu_2OSO_4 under a magnetic field along the three crystallographic directions and uncover the presence of appreciable transverse magnetization which can be probed by magnetic torque measurements. We shall also study the effect of quantum fluctuations and confirm that the reduction of the spin length is indeed very small, in agreement with experiment. Finally, we shall present the magnon band structure from linear spin-wave calculations.

The remainder of the paper is organized as follows. In Sec. II, we highlight the main aspects of the crystal structure of Cu_2OSO_4, including the global symmetries, the different coordination of the two types of Cu ions, and their lattice topology. In Sec. III, we discuss details of DFT calculations (Sec. III A) and the resulting electronic structure (Sec. III B), which sheds light onto the nature of the magnetic orbitals of the two types of Cu sites in Cu_2OSO_4. In Sec. IV, we present our study of the effect of isotropic Heisenberg

interactions, the predicted hierarchy of energy scales from DFT (Sec. IV A), the resulting picture for the infinite classical ground-state manifold, and its close similarity to the 2D kagome Heisenberg AFM (KHAFM; Sec. IV B), and the effect of the interlayer couplings (Sec. IV C). In Sec. V, we present what happens when we include the microscopic DM interactions. This includes an analysis of the constraints imposed by symmetry on the DM vectors (Sec. V A), their numerical values from DFT (Sec. V B), the resulting picture for the structure of the selected ground states (Sec. V C), and a comparison with experiments. In Sec. VI, we incorporate the symmetric part of the exchange anisotropy tensors, discuss their constraints from symmetry (Sec. VI A), identify particular elements of these tensors that can turn the total moment along the observed direction (Sec. VI B), and present DFT results on one of the relevant bonds that corroborate this picture (Sec. VI C). In Sec. VI D, we show more generally that the rotation of the total moment proceeds via a two-step reorientation transition and discuss the evolution of the spin gap through this transition. In Sec. VII, we study some additional topics and make predictions for further experiments: The response of Cu_2OSO_4 under a magnetic field along the three crystallographic directions (Sec. VII A), the effect of quantum fluctuations at the quadratic level (Sec, VIII), the associated reduction of the spin length (Sec. VIII A), and the magnon band structure (Sec. VIII B). In Sec. IX, we give our conclusions and a broader perspective of our work. Finally, we include Appendixes A and B, which contain technical details and auxiliary information.

II. MAIN STRUCTURAL AND SYMMETRY ASPECTS

Figure 1(a) shows the kagomelike structure of each ab layer of Cu_2OSO_4, and Fig. 1(b) shows the way such layers arrange along the c^* axis. There are two symmetry-nonequivalent Cu^{2+} sites in Cu_2OSO_4, denoted as Cu1 and Cu2. The NN Cu2 sites form dimers, whereas Cu1 sites form one-dimensional (1D) chains along the **b** axis. Thus, each layer can be thought of as either a system of chains joined through dimers or a kagome lattice with every third spin replaced by a dimer. The overall spin lattice can be described in terms of the underlying monoclinic Bravais lattice, plus a basis of four atoms, two Cu1 and two Cu2, see Fig. 1.

Cu_2OSO_4 crystallizes in a monoclinic crystal system belonging to the space group $C2/m$ [16], where the monoclinic **c** axis forms an angle of $\beta = 122.34°$ with the **a** axis. The vector c^* is perpendicular to the ab plane, as shown below:

$$ \begin{array}{l} \alpha = \gamma = 90° \\ \beta = 122.34° \end{array} \qquad (1) $$
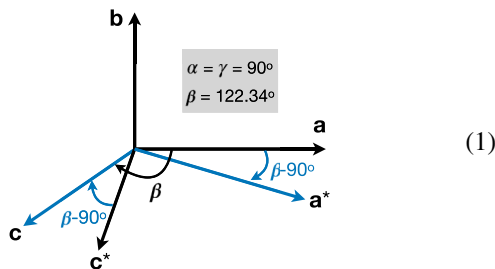
Apart from primitive translations, the $C2/m$ symmetry group includes (i) an inversion center in the middle of the Cu2 dimers, (ii) an inversion center in the middle of the $J_{\perp,2}$ bond,

(iii) a twofold rotation axis $C_{2\mathbf{b}}$ passing through the middle of the Cu2 dimers, (iv) a screw axis along the Cu1 chain corresponding to a nonprimitive translation by **b**/2 followed by a twofold rotation $C_{2\mathbf{b}}$ around the **b** axis, and (v) an ac^* mirror plane that goes through the midpoints of NN Cu1 (or J_3) bonds and includes the Cu2 dimers. The experimental magnetic structure does not break any of these symmetries (it belongs to the irrep Γ_1 of the $C2/m$ space group at zero momentum [22]).

Another important aspect of the Cu_2OSO_4 structure concerns the local coordination of the two types of Cu^{2+} ions, which affects the choice of the magnetic orbital. The Cu1 atoms are surrounded by four oxygen atoms with the Cu–O distances of 2×1.882 Å (Cu1–O3) and 2×2.070 Å (Cu1–O4), see Fig. 2(d). Two further oxygen atoms are located 2.526 Å away from copper and belong to the SO_4 groups. Therefore, Cu1 has $4 + 2$ oxygen coordination with a square plaquette of the four nearest oxygen atoms obtained by an axial elongation of the CuO_6 octahedron. By contrast, Cu2 features two short Cu2–O2 distances of 1.907 Å followed by three further oxygens at 2.000 Å (Cu2–O3) and 2×2.155 Å (Cu2–O4), resulting in $2 + 3$ trigonal-bipyramidal coordination. This structural configuration gives rise to a rather unusual coupling regime that we discuss in the following.

III. DFT AND ELECTRONIC STRUCTURE

A. Methods

DFT band-structure calculations were performed with FPLO [26] and VASP codes [27,28] using the Perdew-Burke-Ernzerhof (PBE) flavor of the exchange-correlation potential [29]. Correlation effects in the Cu 3d shell were considered on the mean-field DFT+U level with the on-site Coulomb repulsion $U_d = 8.5$ eV (FPLO) or 9.5 eV (VASP), Hund's coupling $J_d = 1$ eV, and atomic limit for the double-counting correction [30,31]. Note that U_d is applied to the Cu 3d orbitals; hence, there is usually a difference in the optimal U_d value depending on the DFT code and its basis set [32]. Experimental structural parameters from Ref. [17] were used in all calculations. The various microscopic spin interactions, including the Heisenberg exchange parameters presented below in Sec. IV, the DM vectors (Sec. V), and the symmetric exchange anisotropy $\mathbf{T}_3$ (Sec. VI), have been obtained by a mapping procedure [33,34] from total energies of magnetically ordered states. These energies were converged on a k mesh with 64 points in the first Brillouin zone (BZ) for supercells with 64 atoms (double the crystallographic unit cell of Cu_2OSO_4).

Each interaction parameter is derived from total energies of four spin configurations as follows:

$$ J_{12} = \frac{E_{\uparrow\uparrow} - E_{\uparrow\downarrow} - E_{\downarrow\uparrow} + E_{\downarrow\downarrow}}{4S^2}, \qquad (2) $$

where $S = \frac{1}{2}$ and $\uparrow\uparrow, \uparrow\downarrow, \downarrow\uparrow, \downarrow\downarrow$ denote spin arrangements on interacting atoms 1 and 2, while spins on all other atoms are kept fixed to a globally FM configuration. The $\alpha\beta$ component of the interaction tensor $\mathbb{J}$ is obtained in a similar way by setting the spin on atom 1 along α and the spin on atom 2 along β, whereas the spins on all other atoms are kept along γ perpendicular to both α and β. When $\alpha \neq \beta$, the resulting
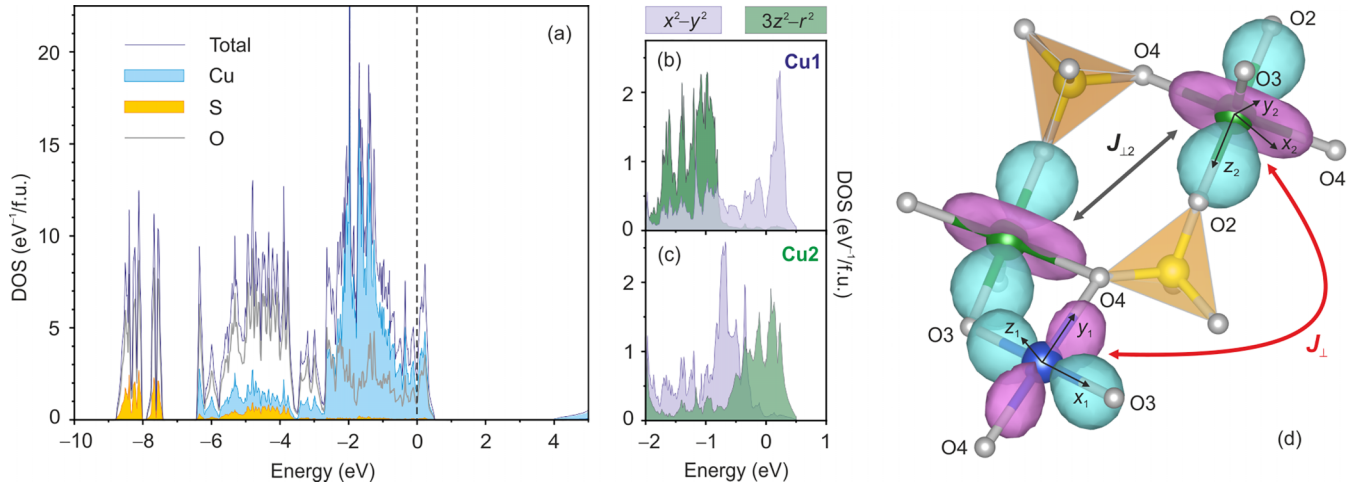
FIG. 2. (a) Electronic density of states (DOS) for Cu_2OSO_4 calculated on the PBE level shows predominant Cu $3d$ states near the Fermi level, which is denoted by the dashed line at zero energy. (b) and (c) Orbital-resolved DOS indicates different symmetry of the magnetic orbitals for the Cu1 and Cu2 atoms. (d) Magnetic orbitals visualized using Wannier functions and superexchange pathways for the interlayer couplings $J_\perp$ and $J_{\perp 2}$. Local coordinate frames for the Cu1 and Cu2 atoms are also shown. The notation of oxygen positions follows Ref. [17].

component is a combination of the DM interaction (D^γ) and off-diagonal symmetric anisotropy ($T^{\alpha\beta}$) that are separated as

$$\epsilon_{\alpha\beta\gamma} D^\gamma = \frac{\mathbb{J}^{\alpha\beta} - \mathbb{J}^{\beta\alpha}}{2}, \qquad (3)$$

$$T^{\alpha\beta} = \frac{\mathbb{J}^{\alpha\beta} + \mathbb{J}^{\beta\alpha}}{2}, \qquad (4)$$

where $\epsilon_{\alpha\beta\gamma}$ is the Levi-Civita symbol.

The FPLO values are for the Heisenberg exchange parameters only because noncollinear spin configurations are not implemented in this DFT code. Additional data related to the DFT results of this paper can be found in Ref. [35].

B. Electronic structure

The uncorrelated (PBE) band structure of Cu_2OSO_4 shows predominantly oxygen states below -3 eV followed by Cu $3d$ bands that extend to slightly above the Fermi level, see Fig. 2(a). The band structure is metallic because correlations in the Cu $3d$ shell have not been included in the calculation. The states near the Fermi level show contributions from both the $d_{x^2-y^2}$ and $d_{3z^2-r^2}$ orbitals, although only one of them should be eventually half-filled and magnetic in the $3d^9$ Cu^{2+} ion. Choosing the x_1 and y_1 local coordinate axes along the shorter Cu1–O3 and Cu1–O4 bonds within the square plaquette results in a separation of the two orbitals, with the $d_{x^2-y^2}$ states lying at higher energies than the $d_{3z^2-r^2}$ ones, see Fig. 2(b). Therefore, $d_{x^2-y^2}$ is the likely magnetic orbital for Cu1. A similar separation is possible in the case of Cu2, but here, the local z_2 axis must be directed along the two shortest Cu2–O2 bonds. The $d_{3z^2-r^2}$ states are then higher in energy than the $d_{x^2-y^2}$ ones, and $d_{3z^2-r^2}$ is the likely magnetic orbital for Cu2, see Fig. 2(c).

This analysis is verified by DFT+U calculations that produce an insulating solution. Correlations stabilize the orbital state with the unpaired electron on the $d_{x^2-y^2}$ orbital for Cu1 and on the $d_{3z^2-r^2}$ orbital for Cu2. This is like the high-temperature phase of another kagomelike mineral volborthite

[36,37] but different from the majority of other Cu-based kagome magnets, including francisite [23], where both Cu sites feature $d_{x^2-y^2}$ as the magnetic orbital.

IV. ISOTROPIC MODEL

We begin our analysis with an investigation of the isotropic Heisenberg spin Hamiltonian:

$$\mathcal{H}_{iso} = \sum_{i<j} J_{ij} \mathbf{S}_i \cdot \mathbf{S}_j, \qquad (5)$$

where J_{ij} denotes the exchange parameter between spin-$\frac{1}{2}$ operators $\mathbf{S}_i$ and $\mathbf{S}_j$ at Cu sites i and j, respectively.

A. DFT results for Heisenberg exchange parameters

Exchange couplings for all Cu–Cu pairs with distances up to 7 Å were calculated using supercells doubled either in the ab plane or along the c direction. The two complementary DFT codes produced consistent results except for the coupling J_1 that is twice as large in VASP as in FPLO. Both sets of parameters will be considered in the following. The leading Heisenberg exchange couplings are listed in Table I and are indicated in Fig. 1. Further exchange couplings can be neglected in the minimal model because they are less than 10 K. Figure 3 shows that the six leading couplings considered in this paper allow a good description of total energies for different spin configurations in Cu_2OSO_4.

The coupling on the Cu2 dimers, which is denoted by J_d, sets the dominant energy scale and is FM. The NN coupling on the Cu1 chains, which is denoted by J_3, is AFM and gives the second strongest energy scale. The couplings J_1 and J_2 between Cu1 and Cu2 ions are also AFM and compete with J_3. Finally, there are two types of interlayer interactions $J_\perp$ and $J_{\perp 2}$, which couple two Cu1 atoms to a single Cu2 atom and two Cu2 atoms to a single Cu2 atom, respectively. The predominance of these couplings over other possible superexchange pathways between the kagome layers can be explained

TABLE I. Microscopic magnetic parameters of Cu_2OSO_4: Leading exchange couplings J_i (in K) obtained from FPLO ($U_d = 8.5$ eV) and VASP ($U_d = 9.5$ eV), and corresponding DM vectors $\mathbf{D}_{ij}$ (VASP), calculated for each bond type. Here, the labeling of the two sites (i and j) of each bond follows the notation of Table III. Note that inversion symmetry forbids the DM interactions on the J_d and $J_{\perp 2}$ bonds.

Bond type	Site i	Site j	$\mathbf{r}_j - \mathbf{r}_i$ (abc^* frame, in Å)	$|\mathbf{r}_j - \mathbf{r}_i|$ (Å)	J_{ij}^{FPLO} (K)	J_{ij}^{VASP} (K)	$\mathbf{D}_{ij}$ (abc^* frame, in K)
J_d (Cu2–Cu2)	Cu22	Cu22p	(0.4322, 0, −2.8166)	2.849	−199	−168	$\mathbf{D}_d = 0$
J_1 (Cu1–Cu2)	Cu11	Cu22	(2.1264, 1.5798, 1.4083)	3.000	20	48	$\mathbf{D}_1 = (43, -39, -38)$
J_2 (Cu1–Cu2)	Cu11	Cu22p	(2.5586, 1.5798, −1.4083)	3.320	66	56	$\mathbf{D}_2 = (-31, 25, -30)$
J_3 (Cu1–Cu1)	Cu11	Cu14	(0, 3.1595, 0)	3.159	74	72	$\mathbf{D}_3 = (15, 0, 81)$
$J_{\perp 2}$ (Cu2–Cu2)	Cu22	Cu23	(1.0307, −3.1595, 3.6375)	4.927	15	15	$\mathbf{D}_{\perp,2} = 0$
$J_\perp$ (Cu1–Cu2)	Cu11	Cu23 + $\mathbf{b}/2$	(3.1572, 1.5798, 5.0458)	6.158	28	26	$\mathbf{D}_\perp = (5, -1, -3)$

by the presence of bridging SO_4 tetrahedra, as shown in Fig. 2(d). The interlayer couplings are weaker than J_2 and J_3 but overall significant. Here, $J_{\perp 2}$ is nonfrustrated and, at first glance, would couple the layers antiferromagnetically. On the other hand, $J_\perp$ forms triangular loops with J_3 in the same way as J_1 does. The coupling $J_\perp$ would not be satisfied in the scenario of simple AFM order imposed by $J_{\perp 2}$. In the experimental magnetic structure, the $J_{\perp 2} - J_{\perp 2} - J_3$ triangles end up having the same type of canted order as the $J_1 - J_1 - J_3$ triangles, so $J_{\perp 2}$ may act as an additional driving force of the canted order, see detailed analysis in Sec. IV B.

Let us now compare the experimentally measured values of the Curie-Weiss temperature Θ_{CW} to the values obtained from the DFT Heisenberg couplings of Table I and the expression (see discussion in Appendix B):

$$\Theta_{\text{CW}} = -\frac{1}{8}[J_d + 2(J_3 + J_{\perp,2}) + 4(J_1 + J_2 + J_\perp)], \quad (6)$$

where the sign convention of Θ_{CW} corresponds to the Curie-Weiss approximation for the susceptibility $\chi = \frac{C}{T - \Theta_{\text{CW}}}$, and C is the Curie constant. The resulting values are provided in the first four rows of the second column of Table II where, for comparison, we give the values corresponding to VASP and FPLO as well as the values without (2D) and with (3D) the interlayer couplings ($J_\perp$ and $J_{\perp,2}$) included. The experimentally
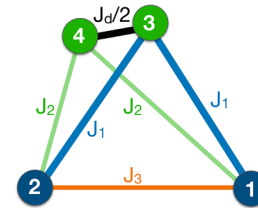
reported values are −68 K for a powder sample [21] and −71, −75, and −70 K along the **a**, **b**, and **c*** axes, respectively, for a single crystal [22]). The comparison shows that (i) including the interlayer couplings gives a more satisfactory agreement, and (ii) the VASP values give better agreement than those of FPLO.

B. The isotropic model of a single layer: Highly frustrated magnetism and similarity to the KHAFM

The isotropic limit of a single layer of Cu_2OSO_4 features an infinite number of classical ground states, which are closely related to the ones of the ideal KHAFM [38–41]. To see this, we follow a cluster minimization method (see, e.g., Ref. [42]) and examine the four-site unit cell of the structure.

1. The building block of classical ground states

Let us first rewrite the total Heisenberg energy of a single layer $\mathcal{H}_{\text{iso},1}$ as a sum over contributions from unit cells:

$$(7)$$

where J_d is replaced by $J_d/2$ because this bond is shared by two cells. We have

$$\mathcal{H}_{\text{iso}} = \sum_{\triangle} \mathcal{H}_{\text{iso},\triangle}, \quad (8)$$

where

$$\mathcal{H}_{\text{iso},\triangle} = J_3 \mathbf{S}_1 \cdot \mathbf{S}_2 + (J_1 \mathbf{S}_3 + J_2 \mathbf{S}_4) \cdot (\mathbf{S}_1 + \mathbf{S}_2) + \frac{J_d}{2} \mathbf{S}_3 \cdot \mathbf{S}_4. \quad (9)$$

As it turns out, in the minimum energy configuration, the spins $\mathbf{S}_3$ and $\mathbf{S}_4$ point along the same direction, and the energy reduces to that of an isosceles Heisenberg triangle with competing couplings J_3 and $J_1 + J_2$:

$$\mathcal{H}'_{\text{iso},\triangle} = J_3 \mathbf{S}_1 \cdot \mathbf{S}_2 + (J_1 + J_2)\mathbf{S}_3 \cdot (\mathbf{S}_1 + \mathbf{S}_2) + \frac{J_d S^2}{2}, \quad (10)$$
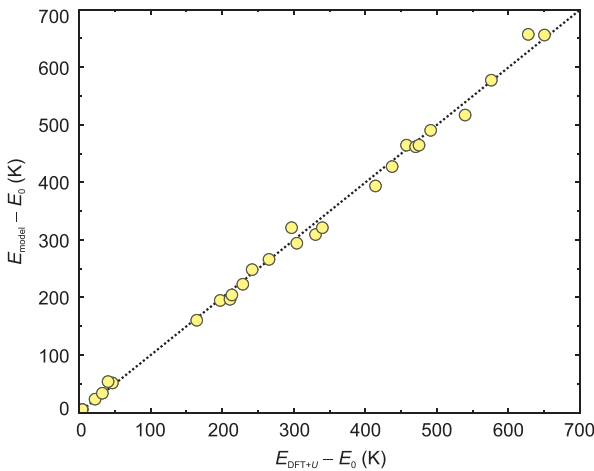

FIG. 3. Comparison of total energies for different spin configurations as evaluated by DFT+U and obtained from the minimal model with six exchange couplings listed in Table I. Both sets of energies are given relative to the reference energy E_0 that corresponds to the nonmagnetic state.

TABLE II. Numerical values of various parameters based on DFT values of microscopic couplings. Different rows correspond to different levels of model descriptions, e.g., $\mathcal{H}_{iso}$ (FPLO, 2D) corresponds to a single layer of Cu$_2$OSO$_4$ with isotropic Heisenberg couplings only, and values given by FPLO code (see Table I), and $\mathcal{H}_{iso} + \mathcal{H}_{DM}$ (VASP, 3D) corresponds to the actual multilayer system, with isotropic and DM couplings (including $J_\perp$, $J_{\perp,2}$, $\mathbf{D}_\perp$, and $\mathbf{D}'_\perp$), and numerical values given by the VASP code. The second column gives the Curie-Weiss temperature Θ_{CW}, which is given by Eq. (6) for the second, fourth, and sixth rows, and by the same equation but with $J_\perp$ and $J_{\perp,2}$ set to zero for the first, third, and fifth rows. For the last two rows, the three values given correspond to Θ_{CW}^{aa}, Θ_{CW}^{bb}, and $\Theta_{CW}^{c^*c^*}$, which are given by Eq. (B17). The vector $\mathbf{m}$ denotes the total moment per Cu site and m its length. For the meaning of the angles θ, α, ψ, and ξ see Eqs. (29)–(31).

Model	Θ_{CW} (K)	Direction of $\mathbf{m}$ (abc^* frame)	m/μ_B ($g=2$)	θ	α	ψ	ξ
$\mathcal{H}_{iso}$ (FPLO, 2D)	−36.6	Any	0.21	54.5°	Any	Any	0
$\mathcal{H}_{iso}$ (FPLO, 3D)	−54.4	Any	0.11	39.6°	Any	Any	0
$\mathcal{H}_{iso}$ (VASP, 2D)	−49.0	Any	0.14	43.8°	Any	Any	0
$\mathcal{H}_{iso}$ (VASP, 3D)	−65.8	Any	0.05	25.5°	Any	Any	0
$\mathcal{H}_{iso} + \mathcal{H}_{DM}$ (VASP, 2D)	−49.0	(0.93, 0, 0.36)	0.22	53.8°	5.0°	90°	11.1°
$\mathcal{H}_{iso} + \mathcal{H}_{DM}$ (VASP, 3D)	−65.8	(0.91, 0, 0.42)	0.22	50.60°	2.60°	90°	10.41°
$\mathcal{H}_{iso} + \mathcal{H}_{DM} + \mathcal{H}_{T_3}$ (VASP, 2D)	(−51.2, −47.8, −48.0)	(0, 1, 0)	0.21	54.39°	3.62°	0	0
$\mathcal{H}_{iso} + \mathcal{H}_{DM} + \mathcal{H}_{T_3}$ (VASP, 3D)	(−68.0, −64.5, −64.8)	(0, 1, 0)	0.19	51.13°	5.2°	0	0

where S is the classical spin length. The minimum energy state takes the schematic form:

$$(11)$$

or more explicitly:

$$\frac{\mathbf{S}_3}{S} = \frac{\mathbf{S}_4}{S} = \mathbf{e}_2 \equiv \mathbf{A},$$

$$\frac{\mathbf{S}_1}{S} = \sin\theta\,\mathbf{e}_1 - \cos\theta\,\mathbf{e}_2 \equiv \mathbf{B}, \qquad (12)$$

$$\frac{\mathbf{S}_2}{S} = -\sin\theta\,\mathbf{e}_1 - \cos\theta\,\mathbf{e}_2 \equiv \mathbf{C},$$

where $\mathbf{e}_1$ and $\mathbf{e}_2$ are any pair of orthogonal axes, and the angle θ can be found by minimizing the energy $E = J_3 \cos(2\theta) - 2(J_1 + J_2)\cos\theta + J_d S^2/2$, which gives

$$\theta = \begin{cases} \cos^{-1}\left(\frac{J_1 + J_2}{2J_3}\right), & \text{if } \frac{|J_3|}{|J_1 + J_2|} \geq \frac{1}{2} \\ 0, & \text{otherwise.} \end{cases} \qquad (13)$$

The values of θ predicted from FPLO and VASP are 54.5° and 43.8°, respectively. From these, the former is closer to the value of 60° realized in the equilateral-triangle limit of $J_1 + J_2 = J_3$, which seems to be the relevant region for Cu$_2$OSO$_4$ [22].

The total magnetic moment per Cu can be obtained by

$$\frac{\mathbf{m}}{g\mu_B} = \frac{S}{2}(1 - \cos\theta)\,\mathbf{e}_2. \qquad (14)$$

Taking $S = \frac{1}{2}$ and assuming $g = 2$, we find $m \simeq 0.21\,\mu_B$ (FPLO) and $0.14\,\mu_B$ (VASP) per Cu. The former is only slightly lower than the value $0.23(3)\,\mu_B$ found experimentally [21]. Thus, at the level of the isotropic model of a single layer, the FPLO values give better agreement for the length of the total moment. This comparison is premature, however, since as we show below (see also fourth column of Table II), these num-

bers show significant variation when including the interlayer couplings and/or the anisotropies.

2. Tilling the ABC state onto the lattice

Having found the ground states of one building block of the Hamiltonian, we can now proceed to tile these on the full lattice. The resulting ground-state manifold consists of infinite ground states, including an infinite subset of coplanar states and an infinite subset of noncoplanar states. Some representative members of this manifold are shown in Fig. 4.

Coplanar states. The uniform coplanar state of Fig. 4(a) is the simplest way to tile the ABC state of Eq. (12) to the full lattice and is the one that has been observed experimentally [22]. This state has an SO(3) order parameter space, as there are two angles needed to fix the planes of **A**, **B**, and **C** and an additional angle to fix the direction of (say) the **A** sublattice within that plane.

However, this is not the only coplanar state. Indeed, starting from the uniform state of Fig. 4(a), one can generate the coplanar state shown in Fig. 4(b) by choosing one of the L horizontal rows of the lattice and swapping $\mathbf{B} \leftrightarrow \mathbf{C}$ along that row. Such an operation does not affect the energetics on the particular row of triangles or on any other triangles of the lattice and is therefore a ground state. Counting all possible sequences of swaps on horizontal chains gives 2^L such coplanar states.

Similar swaps can be performed on nonhorizontal chains as well. However, one cannot perform a sequence of swaps along chains of different direction, so the total degeneracy of coplanar states is 3×2^L (and not 2^{3L}). The uniform state is a special member of this subextensive family of coplanar states.

Noncoplanar states. The above operation of swapping $\mathbf{B} \leftrightarrow \mathbf{C}$ along a given row corresponds to a π rotation of the spins along that row around the direction of the **A** sublattice. This procedure can be generalized to rotations by any angle ϕ. The spins along the given row will rotate around **A** from **B** and **C** to some new directions $\mathbf{B}'$ and $\mathbf{C}'$, which are out of the original ABC plane, see Fig. 4(c). Given that all neighbors of that row of sites point along **A**, a rotation around **A** preserves the local structure and the relative angles necessitated by
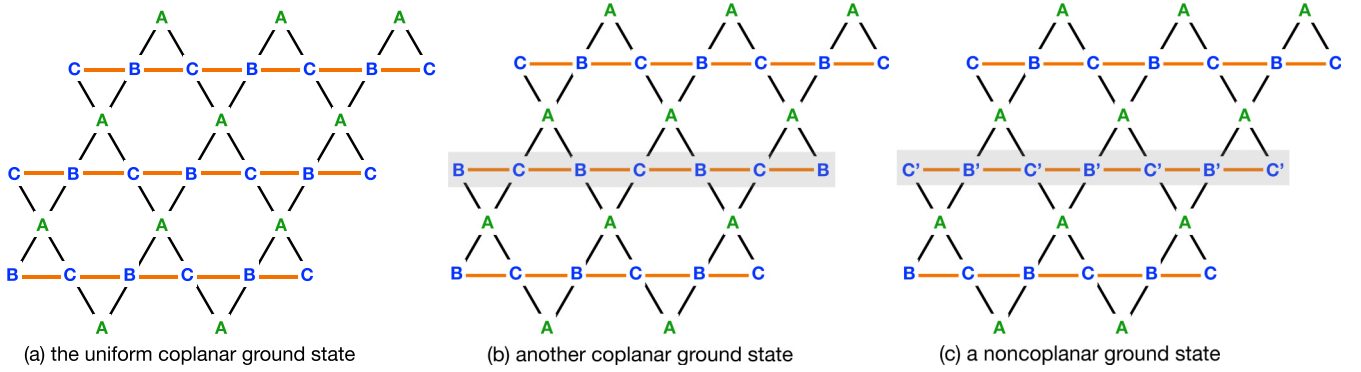
FIG. 4. Representative members of the classical ground-state manifold of the isotropic model of a single layer of Cu_2OSO_4, where Cu2 dimers are represented by one of the three types of vertices of the kagome (**A** sites). (a) The uniform coplanar ABC state, where A, B, and C denote the spin directions of Eq. (12) of the building block of the lattice. (b) One of the 2^L coplanar ground states of a single layer (where L is the number of horizontal rows of the layer). This state results from the one in (a) by swapping **B** ↔ **C** in one of the rows of the layer (shaded). (c) One of the noncoplanar ground states of a single layer. Here, this state results from the one in (a), by rotating the spins belonging to a given row around the direction of **A** by some arbitrary angle ϕ, which effectively rotates **B** and **C** to some new directions **B'** and **C'**, respectively, out of the planes of **A**, **B**, and **C**.

Eqs. (12) and (13) and does not alter the energy. In total, we can perform such a rotation by an angle ϕ_r on the rth row of the lattice, and these angles are generally different, leading to an SO(2) degeneracy for each row [i.e., SO(2)^L in total]. Similar rotations can be performed along the nonhorizontal chains as well.

In addition to the above noncoplanar ground states, one can envisage other ground states which could arise by performing a sequence of rotations along open or closed paths that are different from chains, provided we do not affect the energy of any triangle. While our numerical minimizations show evidence for such more complex ground states, it is not clear whether they belong to the above manifold of noncoplanar states that are generated by performing a sequence of rotations along chains.

Summarizing the physics of the isotropic model on a single layer of Cu_2OSO_4, we have found a classical ground-state manifold with infinite coplanar and infinite noncoplanar ground states, which can all be built from the local three-sublattice building block of Eq. (12). The uniform coplanar state found experimentally is a special member of this manifold. While this state could potentially be the one that is selected by quantum-mechanical fluctuations, we anticipate (based on what happens, e.g., in the case of the KHAFM [39,41,43–46]) that the respective order-by-disorder energy scale is much smaller than the interlayer couplings or the anisotropy. Given that the latter may lift the classical ground-state degeneracy already at the mean-field level, we shall disregard the order by disorder physics of the pure isotropic model and proceed to investigate the effect of the interlayer couplings $J_\perp$ and $J_{\perp,2}$ and the anisotropy.

C. Effect of interlayer couplings

1. Effect of $J_{\perp,2}$ alone

Referring back to the right panel of Fig. 1, one sees that $J_{\perp,2}$ connects one Cu2 dimer from one layer to a Cu2 dimer on the next layer. Thus, the main effect of this interaction is to fix the relative orientation of Cu2 dimers on successive layers,

leading to an alternating **A**, −**A**, **A**, . . . structure of the Cu2 dimers along the $\mathbf{c}^*$ axis.

However, $J_{\perp,2}$ does not lift the infinite degeneracy discussed above, and the system still features infinite coplanar and infinite noncoplanar ground states. For example, we can start from one of the coplanar states in a single layer and then copy its time-reversed version on the next layer and continue in an alternating fashion with the next layers, so that we satisfy $J_{\perp,2}$. However, one can still swap **B** ↔ **C** (or −**B** ↔ −**C**) along any Cu1 chain of any layer without affecting the energy, leading again to a subextensive number of coplanar ground states. The situation for noncoplanar states can be explained in a similar way.

Importantly, none of the members of the classical ground-state manifold matches the one found experimentally because, even when the in-plane configuration is uniform, the relative orientation is AFM across the layers due to $J_{\perp,2}$. Hence, this interaction does not seem to be relevant for the explanation of the uncompensated moment in Cu_2OSO_4.

2. Effect of $J_\perp$ alone

Let us now discuss the effect of $J_\perp$. According to the right panel of Fig. 1, $J_\perp$ connects a NN pair of Cu1 sites on one layer to a Cu2 site on the next layer. Effectively then, this coupling plays a role similar to that of J_1 and J_2, competing with J_3. At the mean-field level, this coupling gives rise to a parallel arrangement of the Cu2 dimers across different layers, in contrast to the antiparallel arrangement favored by $J_{\perp,2}$. Additionally, $J_\perp$ preserves the ABC structure of Eq. (12) of the building block of the lattice but renormalizes the angle θ of Eq. (13) to

$$\theta = \begin{cases} \cos^{-1}\left(\frac{J_1+J_2+J_\perp}{2J_3}\right), & \text{if } \frac{J_3}{J_1+J_2+J_\perp} \geqslant \frac{1}{2} \\ 0, & \text{otherwise,} \end{cases} \quad (15)$$

which arises from Eq. (13) by replacing

$$J_1 + J_2 \mapsto J_1 + J_2 + J_\perp, \quad (16)$$

reflecting the fact that $J_\perp$ plays a similar role to J_1 and J_2, as mentioned above. The *ab initio* parameters of Table I give $\theta \simeq 39.6°$ (FPLO) and 25.5° (VASP), which are further away from the 60° of the equilateral triangle case than the ones without $J_\perp$, see comparison in the fourth column of Table II. In turn, these numbers give a total moment of $m \simeq 0.11 \, \mu_B$ (FPLO) and 0.05 μ_B (VASP) based on Eq. (14), which are significantly reduced compared with the experimental values.

Finally, using the same arguments as in the case of $J_{\perp,2}$ above, one finds that $J_\perp$ also fails to select a unique ground state, and the classical ground-state manifold again contains infinite coplanar and infinite noncoplanar states. The only differences to the case of $J_{\perp,2}$ then are (i) the renormalization of the angle θ and (ii) the fact that now the Cu2 dimers align FM across the layers.

Importantly, the experimentally reported configuration is one of the members of the ground-state manifold, although there is an appreciable deviation in the value of θ. This suggests that either DFT overestimates the value of $J_\perp$ and/or the anisotropic couplings can remedy this problem (see below).

3. Combined effect of $J_\perp$ and $J_{\perp,2}$

Based on the above, the two interlayer couplings compete with each other since $J_\perp$ favors FM alignment of Cu2 dimers across the layers, whereas $J_{\perp,2}$ favors AFM alignment. When both couplings are considered, the numerical minimization of the classical energy on large finite-sized clusters, based on the *ab initio* values of Table I for $J_\perp$ and $J_{\perp,2}$, delivers a unique ground state. This is a coplanar state with eight spin sublattices in total and successive layers arranged antiparallel to each other. The configuration of each layer is uniform with four sublattices. Hence, the combined effect of $J_\perp$ and $J_{\perp,2}$ is to lift the infinite degeneracy completely, but the selected state is not the one found experimentally.

We therefore conclude that the isotropic model of Cu$_2$OSO$_4$ is not enough to account for the experimentally reported state and that further couplings seem to play a qualitative role. In what follows, we then turn to the investigation of the anisotropic interactions in Cu$_2$OSO$_4$, starting from DM anisotropy [24,25].

V. DM INTERACTIONS

We now turn to the effect of DM interactions, which enter the spin Hamiltonian in the general form:

$$\mathcal{H}_{DM} = \sum_{i<j} \mathbf{D}_{ij} \cdot (\mathbf{S}_i \times \mathbf{S}_j), \tag{17}$$

where $\mathbf{D}_{ij}$ is the microscopic DM vector on the bond (ij).

The presence of DM interactions in Cu$_2$OSO$_4$ has been discussed by Takahashi *et al.* [20], who have also estimated an effective (coarse-grained) DM parameter $|\mathbf{D}| \simeq 7$ K, from the value of the magnon gap measured by AFM resonance. Below, we show that this value significantly underestimates the actual size of the DM vectors because (i) not all of the DM components contribute to the magnon gap, and (ii) the latter is affected by the symmetric part of the exchange anisotropy.
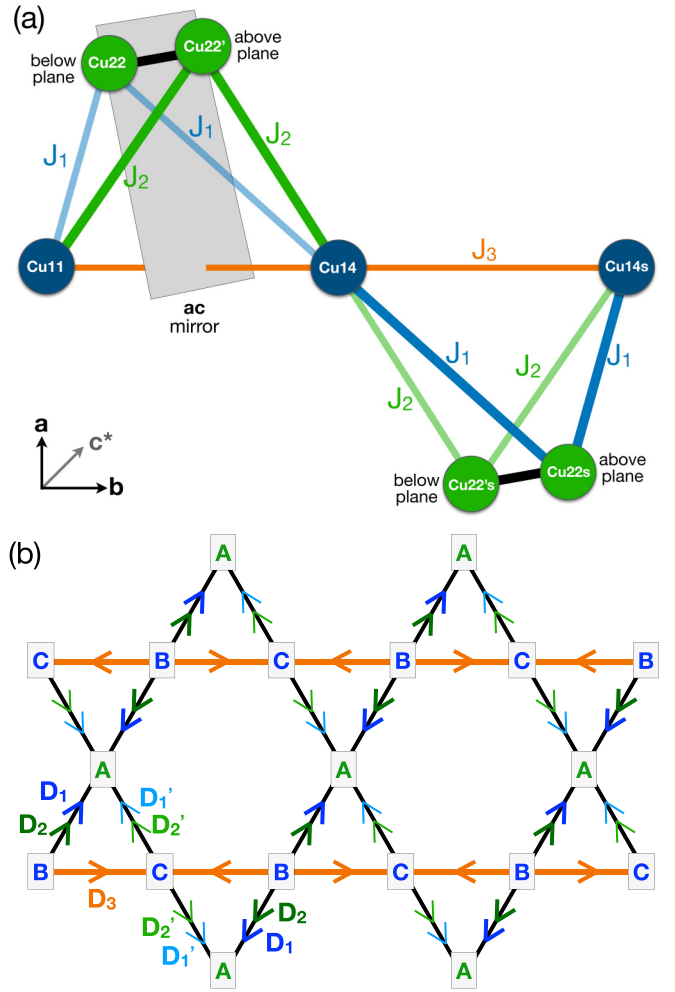

FIG. 5. (a) Local geometry used for the symmetry analysis of the DM vectors, see discussion in the main text. (b) Structure of DM vectors on the layers of Cu$_2$OSO$_4$, where J_1 and J_2 bonds are projected onto each other. Arrows define the sequence of sites (i, j) in the interaction term $\mathbf{D}_{ij} \cdot (\mathbf{S}_i \times \mathbf{S}_j)$. The letters **A**, **B**, and **C** denote the uniform, three-sublattice state found numerically (see text).

A. Constraints from symmetry

Let us first obtain the structure of the DM interactions using symmetry arguments. First of all, the inversion centers on the middle of the J_d and $J_{\perp,2}$ bonds necessitate that the DM vectors on these bonds vanish identically. This leaves the DM vectors on the remaining bonds J_1, J_2, J_3, and $J_\perp$.

Let us consider the local geometry of two neighboring building blocks shown in Fig. 5(a), which shows three consecutive Cu1 sites, labeled as Cu11, Cu14, and Cu14s, and four Cu2 sites (residing on the two adjacent Cu2 dimers), labeled as Cu22, Cu22′, Cu22s and Cu22′s. Now the ac^* mirror plane, which crosses through the midpoint of J_3 bonds and contains the Cu2 dimers, maps $(S^a, S^b, S^{c^*}) \rightarrow (-S^a, S^b, -S^{c^*})$ in spin space. Hence, the DM vectors connected by this operation are related to each other by a π rotation. This implies that the DM vectors on the J_3 bonds lie on the ac^* plane.

Next, let us consider the constraints imposed by the screw axis along **b**, which consists of a C_{2b} rotation in spin-orbit space followed by a translation by **b**/2. This

operation maps Cu11→ Cu14, Cu14→ Cu14s, Cu22→ Cu22s, and Cu22′ → Cu22′s in real space and $(S^a, S^b, S^{c*}) \rightarrow (-S^a, S^b, -S^{c*})$ in spin space. Hence, the DM vectors on any two bonds that are connected by this operation must also be related by a π rotation around **b**.

Altogether, the symmetries impose the following interrelations between the various DM vectors in Fig. 5(a):

$$\mathbf{D}_{11,14} \equiv \mathbf{D}_3, \quad \mathbf{D}_{14,14s} = -\mathbf{D}_3$$

$$\mathbf{D}_{11,22} = \mathbf{D}_{14s,22s} \equiv \mathbf{D}_1, \quad \mathbf{D}_{14,22} = \mathbf{D}_{14,22s} = \mathbf{D}'_1, \quad (18)$$

$$\mathbf{D}_{11,22'} = \mathbf{D}_{14s,22's} \equiv \mathbf{D}_2, \quad \mathbf{D}_{14,22'} = \mathbf{D}_{14,22's} = \mathbf{D}'_2,$$

with $D_3^b = 0$, and

$$\mathbf{D}'_1 \equiv \left(-D_1^a, D_1^b, -D_1^{c*}\right), \quad \mathbf{D}'_2 \equiv \left(-D_2^a, D_2^b, -D_2^{c*}\right). \quad (19)$$

The above relations lead to the sign structure of the DM vectors shown in Fig. 5(b).

Similarly, the DM vectors $\mathbf{D}_\perp$ and $\mathbf{D}'_\perp$ connecting two NN Cu1 sites with a Cu2 site on the next layer [see Fig. 1(b)] are related to each other by the ac^* mirror plane, and therefore,

$$\mathbf{D}'_\perp = (-D_\perp^a, D_\perp^b, -D_\perp^{c*}). \quad (20)$$

1. Insights from cluster decomposition

Like what we did in Eq. (8), we can rewrite the total DM energy as a sum over contributions from the building blocks of Fig. 5(a), namely,

$$\mathcal{H}_{\mathrm{DM}} = \sum_{\triangle} \mathcal{H}_{\mathrm{DM},\triangle}, \quad (21)$$

with

$$\mathcal{H}_{\mathrm{DM},\triangle} = \mathbf{D}_3 \cdot \mathbf{S}_1 \times \mathbf{S}_2 + \mathbf{D}_1 \cdot \mathbf{S}_1 \times \mathbf{S}_3 + \mathbf{D}_2 \cdot \mathbf{S}_1 \times \mathbf{S}_4$$
$$+ \mathbf{D}'_1 \cdot \mathbf{S}_2 \times \mathbf{S}_3 + \mathbf{D}'_2 \cdot \mathbf{S}_2 \times \mathbf{S}_4. \quad (22)$$

As we shall see in Sec. V C, the classical ground state of the lattice model (with Heisenberg and DM couplings included) is a uniform, three-sublattice state, like the state of Eq. (11), with all Cu2 sites parallel to each other due to the strong J_d coupling. We can use this result and replace $\mathbf{S}_4 \mapsto \mathbf{S}_3$ in Eq. (22) to obtain the simpler expression:

$$\mathcal{H}'_{\mathrm{DM},\triangle} = \mathbf{D}_3 \cdot \mathbf{S}_1 \times \mathbf{S}_2 + \mathbf{D}_{1,3}^{\mathrm{eff}} \cdot \mathbf{S}_1 \times \mathbf{S}_3 + \mathbf{D}_{2,3}^{\mathrm{eff}} \cdot \mathbf{S}_2 \times \mathbf{S}_3,$$
$$(23)$$

where

$$\mathbf{D}_{1,3}^{\mathrm{eff}} = \mathbf{D}_1 + \mathbf{D}_2, \quad \mathbf{D}_{2,3}^{\mathrm{eff}} = \mathbf{D}'_1 + \mathbf{D}'_2. \quad (24)$$

One can also incorporate the contribution from the interlayer DM couplings by simply replacing these expressions with

$$\mathbf{D}_{1,3}^{\mathrm{eff}} = \mathbf{D}_1 + \mathbf{D}_2 + \mathbf{D}_\perp, \quad \mathbf{D}_{2,3}^{\mathrm{eff}} = \mathbf{D}'_1 + \mathbf{D}'_2 + \mathbf{D}'_\perp. \quad (25)$$

The above tells us that, due to the strong FM coupling J_d on the Cu2 dimers, out of the six DM vectors $\mathbf{D}_1$, $\mathbf{D}_2$, $\mathbf{D}'_1$, $\mathbf{D}'_2$, $\mathbf{D}_\perp$, and $\mathbf{D}'_\perp$, only the combinations $\mathbf{D}_1 + \mathbf{D}_2 + \mathbf{D}_\perp$ and $\mathbf{D}'_1 + \mathbf{D}'_2 + \mathbf{D}'_\perp$ matter for the low-energy description of Cu$_2$OSO$_4$, along with $\mathbf{D}_3$. As we show in the next subsection, when combined with our DFT results for the DM vectors, this is a key aspect for the understanding of the observed anisotropy in Cu$_2$OSO$_4$.

B. Insights from DFT calculations

The DM vectors calculated using the VASP code are provided in the last column of Table I. The results show large DM vectors for all of the J_1, J_2, and J_3 bonds. The fact that these vectors are comparable in size to the Heisenberg terms seems quite unusual and can be traced back to the close competition between the $d_{x^2-y^2}$ and $d_{3z^2-r^2}$ magnetic orbitals. Microscopically, DM interactions can be understood as the effect of electron hoppings between the nonmagnetic (empty/filled) and magnetic (half-filled) d orbitals in the presence of spin-orbit coupling [25,47]. By fitting the energy bands between -1 and $+0.5$ eV with a tight-binding model containing two orbitals ($d_{x^2-y^2}$ and $d_{3z^2-r^2}$) on each of the Cu sites, we find that such hoppings are comparable in size with hoppings between the magnetic orbitals. For example, we find $t_2 = -0.136$ eV for the hopping between $d_{x^2-y^2}$ of Cu1 and $d_{3z^2-r^2}$ of Cu2 (magnetic-to-magnetic) vs $t'_2 = 0.131$ eV for the hopping between $d_{x^2-y^2}$ of Cu1 and $d_{x^2-y^2}$ of Cu2 (magnetic-to-nonmagnetic). This would still lead to $|\mathbf{D}|/J < 1$, but the Heisenberg term can be further lowered by a FM contribution in the close-to-90° coupling geometry [48], and DM interactions can eventually be favored over isotropic exchange.

Finally, in addition to the DM vectors on the J_1, J_2, and J_3 bonds, there also exists an interlayer DM interaction that lives on the $J_\perp$ bonds, which is however much weaker (see Table I) than the remaining anisotropies.

There are two main insights from the DFT results. First, the strongest DM component is that of $\mathbf{D}_3$ along the c^* axis, $D_3^{c*} = 81$ K. Second, the effective DM vectors connecting Cu1 and Cu2 sites are, according to Eq. (24),

$$2\mathrm{D}: \mathbf{D}_{1,3}^{\mathrm{eff}} = (12, -14, -68)\,\mathrm{K}, \quad \mathbf{D}_{2,3}^{\mathrm{eff}} = (-12, -14, 68)\,\mathrm{K}, \quad (26)$$

or according to Eq. (25), which includes the effect of the interlayer DM vectors,

$$3\mathrm{D}: \mathbf{D}_{1,3}^{\mathrm{eff}} = (17, -15, -71)\,\mathrm{K}, \quad \mathbf{D}_{2,3}^{\mathrm{eff}} = (17, -15, 71)\,\mathrm{K}. \quad (27)$$

Either way, these vectors have a very large component along c^* (± 68 K), like $\mathbf{D}_3$. Hence, we anticipate that the main effect of the DM interactions is to align the spins almost entirely on the ab plane, which is consistent with experiment. Another effect is to increase the angle 2θ between NN Cu1 spins beyond the value given by Eqs. (13) and (15), as the DM favors a 90° orientation.

Turning to the much weaker in-plane DM components, their role is to fix the orientation of the spin structure within the ab plane and additionally give rise to a weak canting of the spins out of that plane. The specifics of these effects will be examined in Sec. V C.

C. Classical ground state

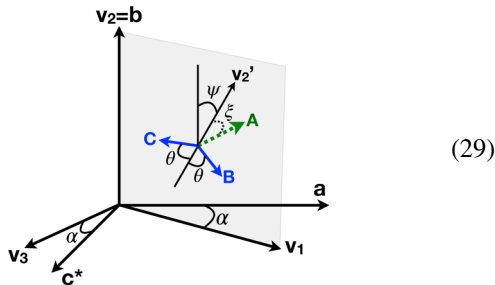#### 1. Results from cluster decompositions and unconstrained minimizations

Let us return to the cluster decomposition of Eq. (21) and examine the ground state of $\mathcal{H}_{\mathrm{DM},\triangle}$. A numerical

minimization of this four-site cluster delivers a ground state which is like that of Eq. (11) but with one crucial difference: Spins 3 and 4 of the Cu2 dimer show a weak misalignment. Due to the latter, this state cannot be tiled on the lattice, and therefore, the decomposition of Eq. (21) does not help to identify the exact ground state of the full lattice model. We then turn to the second smallest cluster, with two tetrahedral blocks:
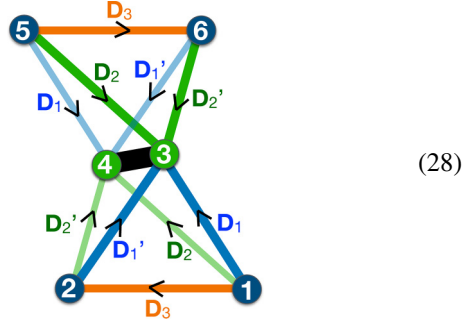
where we have also indicated the direction of the DM vectors on all bonds. The minimum energy configuration of this cluster shows no misalignment between the two spins of the Cu2 dimer (i.e., $\mathbf{S}_4 = \mathbf{S}_3$) and, in addition, $\mathbf{S}_5 = \mathbf{S}_1$ and $\mathbf{S}_6 = \mathbf{S}_2$. This state can be tiled on the lattice, leading to a uniform, three-sublattice state, as shown in Fig. 5(b). This state coincides with the state we find independently via unconstrained numerical minimizations on large finite-sized clusters with periodic boundary conditions.

The three sublattices **A**, **B**, and **C** of the above state can be depicted as

and their directions can be written as follows:

$$\frac{\mathbf{S}_1}{S} = -\cos\theta\,\mathbf{v}_2' + \sin\theta\,\mathbf{v}_1' \equiv \mathbf{B},$$

$$\frac{\mathbf{S}_2}{S} = -\cos\theta\,\mathbf{v}_2' - \sin\theta\,\mathbf{v}_1' \equiv \mathbf{C}, \qquad (30)$$

$$\frac{\mathbf{S}_3}{S} = \frac{\mathbf{S}_4}{S} = \cos\xi\,\mathbf{v}_2' + \sin\xi\,\mathbf{v}_3 \equiv \mathbf{A},$$

where

$$\mathbf{v}_1' = \cos\psi\,\mathbf{v}_1 - \sin\psi\,\mathbf{v}_2,$$

$$\mathbf{v}_2' = \sin\psi\,\mathbf{v}_1 + \cos\psi\,\mathbf{v}_2,$$

$$\mathbf{v}_1 = \cos\alpha\,\hat{\mathbf{a}} + \sin\alpha\,\hat{\mathbf{c}}^*, \qquad (31)$$

$$\mathbf{v}_2 = \hat{\mathbf{b}}, \quad \mathbf{v}_3 = \mathbf{v}_1 \times \mathbf{v}_2.$$

This configuration is qualitatively like the one of Eq. (12). The angle 2θ is the angle between the two Cu1 spins [as in Eq. (12)], the angle α specifies the plane of the Cu1 spins ($\mathbf{S}_1$ and $\mathbf{S}_2$), the angle ψ fixes the overall orientation within that plane, and the angle ξ accounts for a small canting of the Cu2 spins ($\mathbf{S}_3$ and $\mathbf{S}_4$) out of that plane. The state of Eq. (30) reduces to that of Eq. (12) when $\xi = \psi = \alpha = 0$, $\mathbf{v}_1 \to \mathbf{e}_1$, and $\mathbf{v}_2 \to \mathbf{e}_2$.

Let us discuss some further qualitative features of this state:

(i) The state is almost coplanar. The plane of the Cu1 spins lies very close to the ab plane, and the Cu2 sites are tilted slightly away from that plane. Namely, the angles α and ξ are both very small, see the sixth and eighth columns in Table II. This can be traced back to the dominance of the c^* components of $\mathbf{D}_3$, $\mathbf{D}_{1,3}^{\text{eff}}$, and $\mathbf{D}_{2,3}^{\text{eff}}$. Furthermore, our unconstrained numerical minimizations of large clusters show that this result applies to both the single- and multiple-layer cases, with only small quantitative changes when the interlayer interactions are included (energy is lowered slightly, and angles between spins are renormalized).

(ii) The angle 2θ between the two Cu1 spins is larger than the value given by Eqs. (13) and (15), as the DM favors a $90°$ orientation, see the fifth column in Table II.

(iii) The total moment per site is given by (assuming an isotropic **g** tensor, with $g = 2$)

$$\frac{\mathbf{m}}{\mu_{\mathrm{B}}} = S[(\cos\xi - \cos\theta)\,\mathbf{v}_2' + \sin\xi\,\mathbf{v}_3], \qquad (32)$$

which reduces to Eq. (14) for $\xi = 0$ and $\mathbf{v}_2' \to \mathbf{e}_2$. The VASP values of Table I give a total moment per Cu site $m = 0.22\,\mu_{\mathrm{B}}$, for both the single- and multilayer cases (see the fourth column in Table II), which is very close to the experimental value [21,22].

(iv) The direction of the total moment lies in the ac^* plane and predominantly along the **a** axis (see the third column in Table II), and the angle $\psi = \pi/2$. The selection of this direction stems from the in-plane components of the DM vectors. This can be seen more directly by replacing the ansatz of Eq. (30) into the expression for the energy of Eq. (23), which reveals that the terms involving ψ are all proportional to $\sin\psi$, and

$$\frac{d}{d\psi}E'_{\text{DM},\triangle} = 2\cos\psi\sin\xi\left\{\cos\theta\,\left(D_{1,3}^{\text{eff}}\right)^b - \sin\theta\left[\left(D_{1,3}^{\text{eff}}\right)^a\cos\alpha + \left(D_{1,3}^{\text{eff}}\right)^{c^*}\sin\alpha\right]\right\}, \qquad (33)$$

and therefore, the minimum energy corresponds to $\psi = \pm\pi/2$. This result disagrees with experimental data, which show that the total moment is along the **b** axis and not the **a** axis [21,22]. Additionally, this disagrees with the refinement of neutron diffraction data, which delivers a state that belongs

to the identity irrep Γ_1 $C2/m$ at zero momentum [22], while the state favored by the in-plane DM components clearly breaks the ac^* mirror plane and belongs to the Γ_3 irrep.

So the model with Heisenberg and DM couplings included reproduces all experimental data except one, the direction

of the uncompensated moment. According to Eq. (33), this deficiency cannot be remedied within the above model, unless we abandon the major insight from DFT on the separation of energy scales between the out-of-plane and in-plane components of $\mathbf{D}_3$, $\mathbf{D}_{1,3}^{\text{eff}}$, and $\mathbf{D}_{2,3}^{\text{eff}}$. As this ingredient is crucial for getting the remaining aspects of the observed state right, the origin of the disagreement for the direction of the total moment must be sought in some other type of anisotropy, with the symmetric interactions $\mathbf{T}$ being the natural candidate.

The energy scale of this additional anisotropy should be at least as strong as the in-plane components of $\mathbf{D}_3$, $\mathbf{D}_{1,3}^{\text{eff}}$, and $\mathbf{D}_{2,3}^{\text{eff}}$. To get an idea of this energy scale, we have fixed the parameters α, ξ, and θ to the values corresponding to the minimum energy configuration and then tracked the variation of the total energy as we rotate ψ away from $\pm\pi/2$. This calculation delivers a variational bound to the energy cost, which varies within a bandwidth of only ~ 8.77 K as we vary ψ between 0 and 2π. Hence, only a small amount of the additional anisotropy is necessary to rotate the moment along the direction found experimentally.

VI. SYMMETRIC ANISOTROPY T

The symmetric (and traceless) part of the anisotropy $\mathbf{T}$ enters the spin Hamiltonian in the form:

$$\mathcal{H}_T = \sum_{i<j} \mathbf{S}_i \cdot \mathbf{T}_{ij} \cdot \mathbf{S}_j, \qquad (34)$$

where the 3×3 matrices $\mathbf{T}_{ij}$ have the properties $T_{ij}^{\alpha\beta} = T_{ij}^{\beta\alpha}$ (where α and β are Cartesian components) and $\text{Tr}(\mathbf{T}_{ij}) = 0$.

A. Constraints from symmetry

The screw axis along $\mathbf{b}$ dictates that $\mathbf{T}_3$ is uniform along the chains (unlike the DM vector $\mathbf{D}_3$ which is staggered along the chains). Furthermore, the ac^* mirror plane dictates that the only nonzero off-diagonal matrix elements of $\mathbf{T}_3$ are $T_3^{ac^*} = T_3^{c^*a}$ and $T_3^{bc^*} = T_3^{c^*b}$. The same is true for the matrix $\mathbf{T}_d$. By contrast, the matrix elements of $\mathbf{T}_1$ and $\mathbf{T}_2$ in the (abc^*) frame are all nonzero, in principle. Furthermore, the screw axis along $\mathbf{b}$ dictates that the signs of the matrix elements $T_{1,2}^{ab} = T_{1,2}^{ba}$ and $T_{1,2}^{c^*b} = T_{1,2}^{bc^*}$ alternate from one building block of the structure to the next, as we travel along the Cu1 chains. For the bonds of Fig. 5(a), we have, for example,

$$\mathbf{T}_{11,22} \equiv \mathbf{T}_1 = \begin{pmatrix} T_1^{aa} & T_1^{ab} & T_1^{ac^*} \\ T_1^{ab} & T_1^{bb} & T_1^{bc^*} \\ T_1^{ac^*} & T_1^{bc^*} & -T_1^{aa}-T_1^{bb} \end{pmatrix}_{\{a,b,c^*\}}, \quad (35)$$

and

$$\mathbf{T}_{14,22} \equiv \mathbf{T}_1' = \begin{pmatrix} T_1^{aa} & -T_1^{ab} & T_1^{ac^*} \\ -T_1^{ab} & T_1^{bb} & -T_1^{bc^*} \\ T_1^{ac^*} & -T_1^{bc^*} & -T_1^{aa}-T_1^{bb} \end{pmatrix}_{\{a,b,c^*\}}, \qquad (36)$$

and similarly for $\mathbf{T}_{11,22'} \equiv \mathbf{T}_2$ and $\mathbf{T}_{14,22'} \equiv \mathbf{T}_2'$.

B. Identifying the relevant element of the symmetric exchange tensor

Like what we did in Eqs. (8) and (21), we can rewrite the total energy from $\mathbf{T}$ interactions as a sum over contributions from the building blocks of Fig. 5(a), namely,

$$\mathcal{H}_T = \sum_{\triangle} \mathcal{H}_{T,\triangle}, \qquad (37)$$

with

$$\mathcal{H}_{T,\triangle} = \mathbf{S}_3 \cdot \mathbf{T}_d \cdot \mathbf{S}_4 + \mathbf{S}_1 \cdot \mathbf{T}_3 \cdot \mathbf{S}_2 + \mathbf{S}_1 \cdot \mathbf{T}_1 \cdot \mathbf{S}_3 \\ + \mathbf{S}_1 \cdot \mathbf{T}_2 \cdot \mathbf{S}_4 + \mathbf{S}_2 \cdot \mathbf{T}_1' \cdot \mathbf{S}_3 + \mathbf{S}_2 \cdot \mathbf{T}_2' \cdot \mathbf{S}_4. \qquad (38)$$

Anticipating that the strong FM coupling J_d will again enforce parallel (or almost parallel) alignment of the Cu2 spins, we can replace $\mathbf{S}_4 \mapsto \mathbf{S}_3$ in Eq. (38) to obtain the simpler expression:

$$\mathcal{H}_{T,\triangle}' = \mathbf{S}_3 \cdot \mathbf{T}_d \cdot \mathbf{S}_3 + \mathbf{S}_1 \cdot \mathbf{T}_3 \cdot \mathbf{S}_2 \\ + \mathbf{S}_1 \cdot \mathbf{T}_{1,3}^{\text{eff}} \cdot \mathbf{S}_3 + \mathbf{S}_2 \cdot \mathbf{T}_{2,3}^{\text{eff}} \cdot \mathbf{S}_3, \qquad (39)$$

where $\mathbf{T}_{1,3}^{\text{eff}} = \mathbf{T}_1 + \mathbf{T}_2$ and $\mathbf{T}_{2,3}^{\text{eff}} = \mathbf{T}_1' + \mathbf{T}_2'$. In principle, one can also add the contribution from the interlayer couplings ($\mathbf{T}_\perp$, $\mathbf{T}_{\perp,2}$, and their mirror images $\mathbf{T}_\perp'$ and $\mathbf{T}_{\perp,2}'$), but we shall disregard them as they are likely much weaker than $\mathbf{T}_3$, $\mathbf{T}_d$, $\mathbf{T}_{1,3}^{\text{eff}}$, and $\mathbf{T}_{2,3}^{\text{eff}}$.

In the following, we shall set out to identify the components of the $\mathbf{T}$ matrices which favor a rotation of the total moment along the $\mathbf{b}$ axis and, as such, can compete with the in-plane DM components. We shall do this for the matrices $\mathbf{T}_d$ and $\mathbf{T}_3$ that correspond to the bonds with the strongest Heisenberg exchange paths, which are also the ones that lead to simple analytical insights.

1. Effect of $\mathbf{T}_d$

To understand the effect of $\mathbf{T}_d$, we examine its spectrum. The eigenvalues are given by

$$\lambda_1^{(d)} = +T_d^{bb},$$
$$\lambda_2^{(d)} = -\frac{T_d^{bb}}{2} - \sqrt{\left(\frac{T_d^{bb}}{2}\right)^2 + (T_d^{aa})^2 + (T_d^{ac^*})^2 + T_d^{aa}T_d^{bb}},$$
$$\lambda_3^{(d)} = -\frac{T_d^{bb}}{2} + \sqrt{\left(\frac{T_d^{bb}}{2}\right)^2 + (T_d^{aa})^2 + (T_d^{ac^*})^2 + T_d^{aa}T_d^{bb}},$$

$$(40)$$

and the corresponding eigenvectors by

$$\mathbf{u}_1^{(d)} = \hat{\mathbf{b}},$$
$$\mathbf{u}_2^{(d)} = [T_d^{aa} + T_d^{bb} - \lambda_1^{(d)}]\hat{\mathbf{a}} + T_d^{ac^*}\hat{\mathbf{c}}^*, \qquad (41)$$
$$\mathbf{u}_3^{(d)} = [T_d^{aa} + T_d^{bb} - \lambda_2^{(d)}]\hat{\mathbf{a}} + T_d^{ac^*}\hat{\mathbf{c}}^*.$$

It follows that, if $T_d^{bb} < 0$, then the $\mathbf{T}_d$ interaction favors alignment along the $\mathbf{b}$ axis, whereas if $T_d^{bb} > 0$, it favors alignment in the ac^* plane. Thus, the crucial ingredient is the sign of T_d^{bb}.

2. Effect of $\mathbf{T_3}$

By rewriting

$$\mathbf{S}_1 \cdot \mathbf{T}_3 \cdot \mathbf{S}_2 = \frac{1}{2}\mathcal{S}^T \cdot \begin{pmatrix} \mathbf{0} & \mathbf{T}_3 \\ \mathbf{T}_3 & \mathbf{0} \end{pmatrix} \cdot \mathcal{S}, \qquad (42)$$

where $\mathcal{S} = (S_1^a, S_1^b, S_1^{c^*}, S_2^a, S_2^b, S_2^{c^*})^T$, one can understand the effect of $\mathbf{T}_3$ by examining the spectrum of the 6×6 matrix $\begin{pmatrix} \mathbf{0} & \mathbf{T}_3 \\ \mathbf{T}_3 & \mathbf{0} \end{pmatrix}$. Now $\mathbf{T}_3$ has the same form as $\mathbf{T}_d$, so its eigenvalues and eigenstates are, respectively,

$$\lambda_1^{(3)} = +T_3^{bb},$$

$$\lambda_2^{(3)} = -\frac{T_3^{bb}}{2} - \sqrt{\left(\frac{T_3^{bb}}{2}\right)^2 + \left(T_3^{aa}\right)^2 + \left(T_3^{ac^*}\right)^2 + T_3^{aa}T_3^{bb}},$$

$$\lambda_3^{(3)} = -\frac{T_3^{bb}}{2} + \sqrt{\left(\frac{T_3^{bb}}{2}\right)^2 + \left(T_3^{aa}\right)^2 + \left(T_3^{ac^*}\right)^2 + T_3^{aa}T_3^{bb}},$$

$$(43)$$

and

$$\mathbf{u}_1^{(3)} = \hat{\mathbf{b}},$$

$$\mathbf{u}_2^{(3)} = \left[T_3^{aa} + T_3^{bb} - \lambda_1^{(3)}\right]\hat{\mathbf{a}} + T_3^{ac^*}\hat{\mathbf{c}}^*, \qquad (44)$$

$$\mathbf{u}_3^{(3)} = \left[T_3^{aa} + T_3^{bb} - \lambda_2^{(3)}\right]\hat{\mathbf{a}} + T_3^{ac^*}\hat{\mathbf{c}}^*.$$

The desired eigenvalues and eigenvectors of $\begin{pmatrix} \mathbf{0} & \mathbf{T}_3 \\ \mathbf{T}_3 & \mathbf{0} \end{pmatrix}$ can then be expressed in terms of $\lambda_j^{(3)}$ and $\mathbf{u}_j^{(3)}$ (with $j = 1$–3) as

$$\pm\lambda_j^{(3)} \quad \text{and} \quad \left[\mathbf{u}_j^{(3)}, \pm\mathbf{u}_j^{(3)}\right]^T, \qquad (45)$$

respectively. From these results, it follows that the crucial ingredient is the sign of the matrix element T_3^{bb}: If $T_3^{bb} > 0$, the minimum eigenvalue is $\lambda_2^{(3)}$, and the form of the corresponding eigenvector $[\mathbf{u}_2^{(3)}, \mathbf{u}_2^{(3)}]^T$ tells us that the total moment of the two Cu1 spins $\mathbf{S}_1 + \mathbf{S}_2$ must lie on the ab plane. By contrast, if $T_3^{bb} < 0$, the minimum eigenvalue is $\lambda_1^{(3)}$, and the form of the corresponding eigenvector $[\mathbf{u}_1^{(3)}, \mathbf{u}_1^{(3)}]^T$ tells us that $\mathbf{S}_1 + \mathbf{S}_2$ will be aligned with the $\mathbf{b}$ axis and will therefore compete with the in-plane components of the DM vectors. Thus, like the case of $\mathbf{T}_d$, the most relevant aspect of $\mathbf{T}_3$ is the sign of T_d^{bb}.

C. $\mathbf{T_3}$ matrix from DFT and effect on the ground state

Having identified the relevant matrix elements of the symmetric anisotropy, we have carried out DFT calculations based on the VASP code to check if such matrix elements (i) are, in principle, present in Cu_2OSO_4, (ii) have the right sign, and (iii) are strong enough to compete with the in-plane DM components. The results for the J_3 bond:

$$\mathbf{T}_3 = \begin{pmatrix} 8.84 & 0 & 5.77 \\ 0 & -5 & 0 \\ 5.77 & 0 & -3.84 \end{pmatrix}_{\{a,b,c^*\}} \qquad (46)$$

(in K), show that T_3^{bb} is negative and of comparable size with the energy scale required to turn the moment along $\mathbf{b}$, as found experimentally [21,22].

To check this explicitly, we have performed unconstrained numerical minimizations of a single layer of Cu_2OSO_4 using large clusters with periodic boundary conditions and including the Heisenberg, DM, and $\mathbf{T}_3$ couplings delivered by VASP. The results confirm that a T_3^{bb} coupling of the order of -5 K is enough to rotate the total moment along the $\mathbf{b}$ axis, as found experimentally [21,22]. We have also found that the angle ξ, which describes the canting of the Cu2 spins out of the plane of the Cu1 spins, reduces to zero, and the configuration becomes fully coplanar. Additionally, the angle α that describes the tilt of the spin plane away from the ab plane decreases to $3°$–$5°$. Such a small misalignment of the spin plane from the ab plane can be easily missed experimentally. Finally, the total moment per Cu site is $0.21 \mu_B$ and $0.9 \mu_B$ for one and multiple layers, respectively, see Table II. It is likely that the remaining $\mathbf{T}$ couplings will renormalize these numbers slightly, but the agreement to experiment [21,22] is already very satisfactory.

D. Nature of the reorientation process and the spin gap

To uncover the nature of the reorientation transition, we examine the evolution of the classical ground state of the Hamiltonian:

$$\mathcal{H}_\lambda = \mathcal{H}_{iso} + \mathcal{H}_{DM} + \lambda \, \mathcal{H}_{T_3}, \qquad (47)$$

as we vary the rescaling parameter λ from zero to one. The results are summarized in Fig. 6. We find that the reorientation proceeds via two continuous phase transitions, involving an intermediate phase (indicated by shading), where the total moment rotates from predominantly along the $\mathbf{a}$ axis to the $\mathbf{b}$ axis. The boundary between the intermediate phase and the large-λ phase involves the spontaneous breaking of the ac^* mirror symmetry, whereas the boundary to the small-λ phase involves the breaking of the symmetry $\mathcal{T} \times C_{2b}$, where $\mathcal{T}$ is the time reversal and C_{2b} is the π rotation around the b axis in spin space alone; this combined operation flips the b component of all spins.

1. Spin gap

The main curves of Fig. 6 show the evolution of the spin gap through the two-step reorientation process, as obtained from linear spin-wave theory (see further discussion on magnon dispersions in Sec. VIII below). First of all, the value of the spin gap depends very sensitively on λ across the two-step reorientation transition. The spin gap drops to zero at the two boundaries of the intermediate phase. The closing of the gap at these boundaries is related to the spontaneous breaking of the symmetries discussed above.

Away from the intermediate phase, the spin gap reaches ~ 19 and 33 K at $\lambda = 0$ and 1, respectively. These values are set by the energy scales of the in-plane DM components of $\mathbf{D}_3$, $\mathbf{D}_{1,3}^{eff}$, and $\mathbf{D}_{1,3}^{eff}$ and by that of $\mathbf{T}_3$, respectively. The out-of-plane DM components alone do not contribute to the spin gap because, in the absence of the in-plane DM components and $\mathbf{T}_3$, the system has a continuous U(1) symmetry, and the states of Fig. 6 break this symmetry spontaneously. This is shown explicitly in Fig. 8(a), which we discuss in Sec. VIII below.
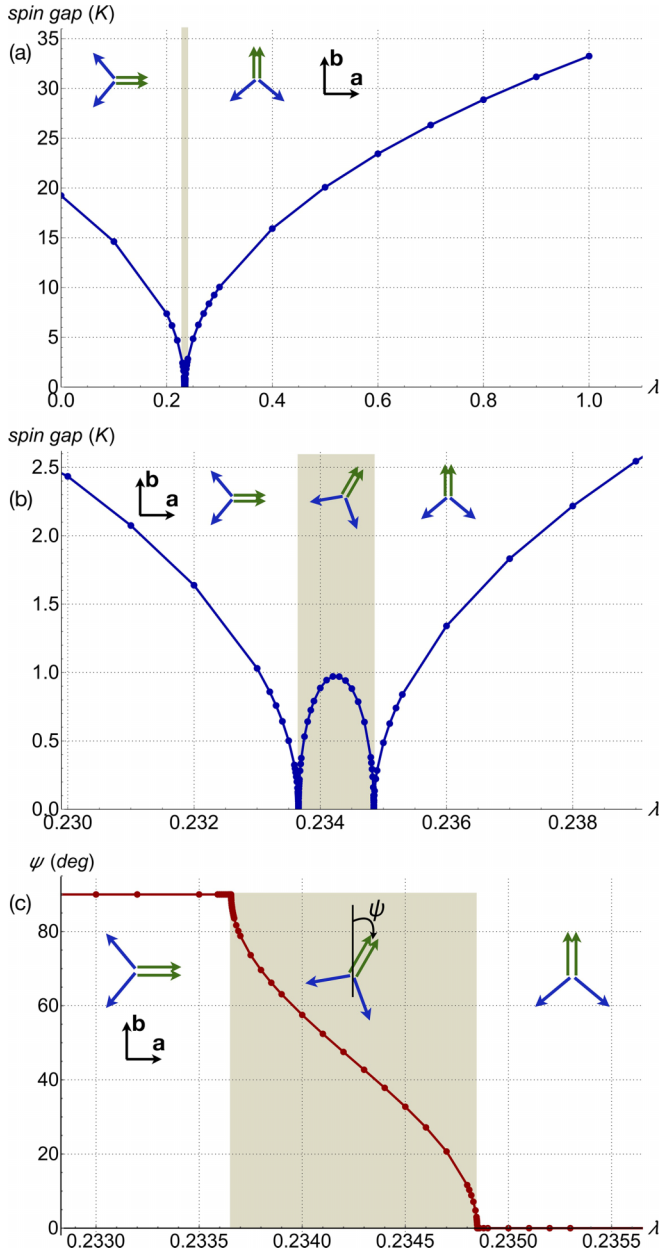
FIG. 6. (a) Evolution of the spin gap with the rescaling parameter λ of Eq. (47), which characterizes the strength of the symmetric anisotropy $\mathbf{T}_3$. (b) Same as in (a) but zooming in the intermediate, reorientation region. (c) Corresponding evolution of the angle ψ, see inset diagrams.

2. Comparison to experiment

Let us now compare the calculated values of the spin gap to the one extracted experimentally from AFM resonance data, which is ~ 1.14 K [20]. This value is much smaller than the calculated gap at $\lambda = 1$. However, one should keep in mind that this value has been measured for a very weak mode that becomes visible below 5.3 K only, i.e., at temperatures much lower than T_N. The nature of this mode must be clarified in future experiments. It is also worth noting that the above Hamiltonian includes the symmetric anisotropy on the J_3 bond only and that the $\mathbf{T}$ couplings on the remaining bonds may

compete with the effect of T_3^{bb}, thereby effectively reducing the spin gap and/or bringing Cu$_2$OSO$_4$ closer to the boundary with the intermediate phase, where the spin gap vanishes.

A related comment is in order here, which may connect the puzzle of the smallness of the observed spin gap with another puzzle that concerns the reported magnetization data for $\mathbf{H} \parallel \mathbf{a}$, see Fig. 5(b) of Ref. [21]. According to these data, m^a shows a small jump at zero field, from about -0.0125 to $+0.0125$ Bohr magnetons per Cu site. One plausible explanation can be the presence of an accidental misalignment of the field toward the **b** axis. Comparing the zero-field jump in m^a for $\mathbf{H} \parallel \mathbf{a}$ with the corresponding jump in m^b for $\mathbf{H} \parallel \mathbf{b}$, this misalignment would amount to only $3°$, which is a plausible explanation. However, an alternative scenario, which could also resolve the puzzle of the smallness of the spin gap, is that the system may actually be slightly inside the intermediate phase. A definite answer to this requires further dedicated experimental studies.

VII. OTHER ASPECTS AND PREDICTIONS FOR FURTHER EXPERIMENTS

A. Magnetization process

To compare with reported magnetization curves, we have also studied the effect of an applied external field $\mathbf{H}$ along the three directions $\mathbf{a}$, $\mathbf{b}$, and $\mathbf{c}^*$. The Zeeman coupling to the field takes the usual form:

$$\mathcal{H}_Z = -g\mu_B \mathbf{H} \cdot \mathbf{S}_{\text{tot}}, \quad \mathbf{S}_{\text{tot}} = \sum_i \mathbf{S}_i, \tag{48}$$

where we have assumed an isotropic $\mathbf{g}$ tensor with $g = 2$.

To find the evolution of the classical ground state of Cu$_2$OSO$_4$ for different field directions and field strengths, we have first performed unconstrained minimizations on large finite-sized clusters with periodic boundary conditions. As it turns out, the state remains uniform for all field strengths. This allows us to decompose $\mathcal{H}_Z$ in terms of contributions from the clusters shown in Eq. (28), namely,

$$\mathcal{H}_Z = \sum \mathcal{H}_{Z,} , \tag{49}$$

with

$$\mathcal{H}_{Z,} = -g\mu_B \mathbf{H} \cdot \left[\tfrac{1}{2}(\mathbf{S}_1 + \mathbf{S}_2 + \mathbf{S}_5 + \mathbf{S}_6) + \mathbf{S}_3 + \mathbf{S}_4 \right], \tag{50}$$

where we use the site labeling of Eq. (28), and the prefactor of $\frac{1}{2}$ in the first term inside the square bracket takes care of double counting. A numerical minimization of this six-site cluster delivers, as before, $\mathbf{S}_4 = \mathbf{S}_3$, $\mathbf{S}_5 = \mathbf{S}_1$ and $\mathbf{S}_6 = \mathbf{S}_2$, which simplifies Eq. (49) to

$$\mathcal{H}_{Z,} = -g\mu_B \mathbf{H} \cdot (\mathbf{S}_1 + \mathbf{S}_2 + 2\mathbf{S}_3). \tag{51}$$

Before we present the numerical results, let us discuss some symmetry aspects. In the absence of a field, the system is invariant under the ac^* mirror symmetry $\mathcal{M}_{ac^*}$ and under
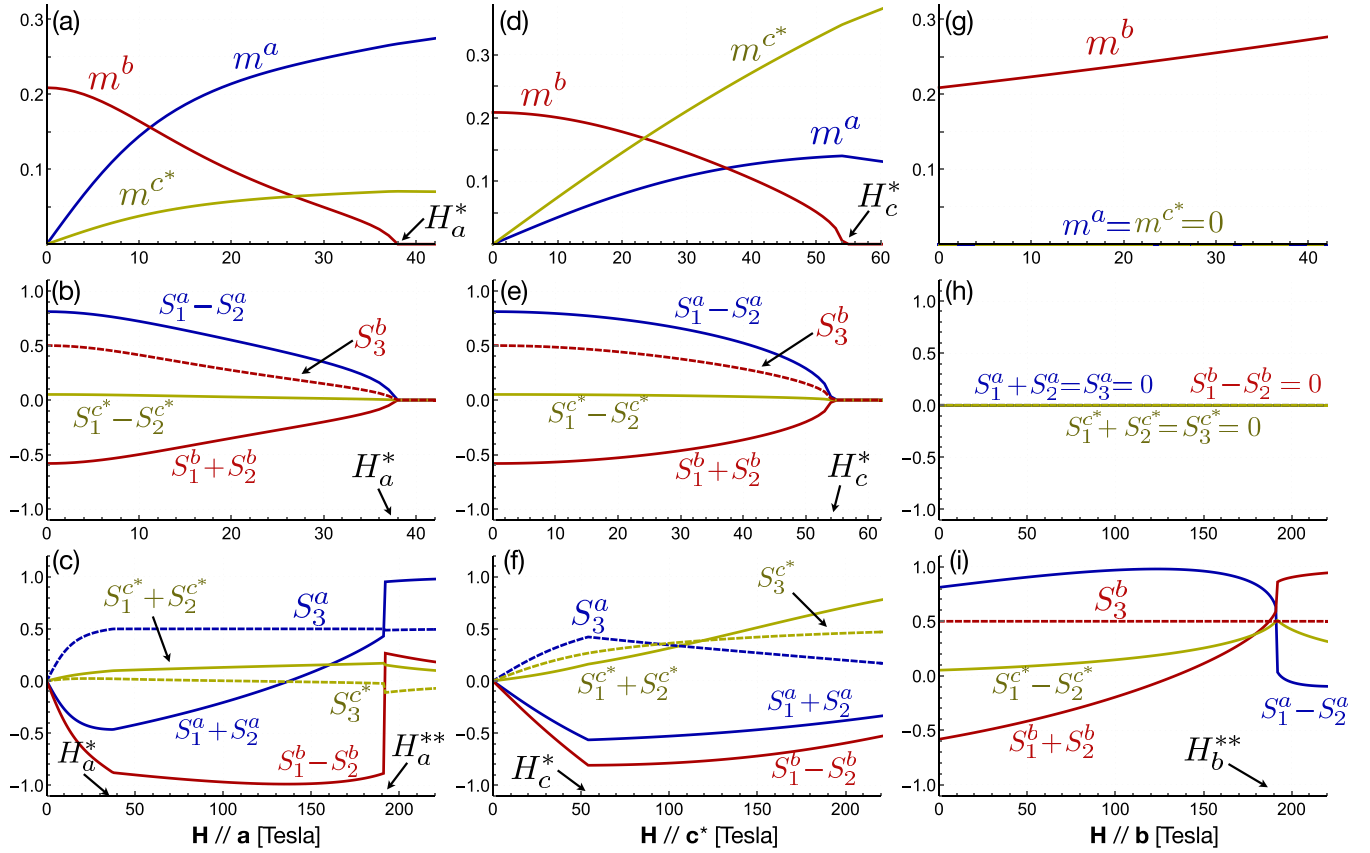
FIG. 7. Evolution of the classical ground state of a single layer of Cu_2OSO_4 as a function of an external magnetic field applied along the (a)–(c) **a** axis, (d)–(f) **c*** axis, and (g)–(i) **b** axis. The results are obtained by numerical minimizations on a single layer of Cu_2OSO_4, using the Hamiltonian $\mathcal{H}_{iso} + \mathcal{H}_{DM} + \mathcal{H}_{T_3} + \mathcal{H}_Z$, see text. The first row of panels shows the three components of the total magnetic moment per Cu site **m** in units of μ_B. (b) and (e) in the second row show the combinations of spin components that play the role of order parameters, which set in at the fields H_a^* and H_c^*. There is no such phase transition for fields along **b**, see (h). The last row shows the combination of spin components which are driven by the field, in a wider field range. The fields H_a^{**} and H_b^{**} correspond to abrupt reorientation of the Cu1 spins, before we reach the saturation fields H_{sat}. There is no such transition for fields along **c***.

the time reversal operation $\mathcal{T}$. Now when the field is along the **a** axis or along the **c*** axis, the system is invariant under the combined operation $\mathcal{M}_{ac^*} \times \mathcal{T}$, which maps

$$\begin{aligned}
\left(S_1^a, S_1^b, S_1^{c^*}\right) &\rightarrow \left(S_2^a, -S_2^b, S_2^{c^*}\right), \\
\left(S_3^a, S_3^b, S_3^{c^*}\right) &\rightarrow \left(S_3^a, -S_3^b, S_3^{c^*}\right).
\end{aligned} \quad (52)$$

The classical ground states are found to break this symmetry spontaneously at a finite field H^*, below which the system shows the following nonzero order parameters: $S_1^a - S_2^a$, $S_1^b + S_2^b$, $S_1^{c^*} - S_2^{c^*}$, and S_3^b.

By contrast, in the presence of the field along the **b** axis, the ac^* mirror plane survives, which means that the states related by the transformation:

$$\begin{aligned}
\left(S_1^a, S_1^b, S_1^{c^*}\right) &\leftrightarrow \left(-S_2^a, S_2^b, -S_2^{c^*}\right), \\
\left(S_3^a, S_3^b, S_3^{c^*}\right) &\rightarrow \left(-S_3^a, S_3^b, -S_3^{c^*}\right),
\end{aligned} \quad (53)$$

have the same energy. In principle, the classical ground states could break this symmetry spontaneously, but this is not supported by our numerics (the associated order parameters, which, in this case, are $S_1^a + S_2^a$, $S_1^b - S_2^b$, $S_1^{c^*} + S_2^{c^*}$, S_3^a, and $S_3^{c^*}$, all vanish irrespective of the field strength).

Our numerical minimization data shown in Fig. 7 give insights into the evolution of the classical ground state of a single layer of Cu_2OSO_4 as a function of an external magnetic field along **a** [panels (a)–(c)], **c*** (d)–(f), and **b** (g)–(i). The results for the multilayer case are qualitatively the same. The first row of panels shows the evolution of the three components of the total magnetic moment per Cu, **m**. The second row shows the combinations of Eqs. (52) and (53) which, as discussed above, play the role of order parameters. Finally, the last row shows the combination of spin components which are driven explicitly by the field and their evolution in a wider field range. Let us discuss the main features of Fig. 7:

(1) Unlike the case of a field along **b** [panel (g)], a field along **a** [panel (a)] and/or **c*** [panel (d)] can induce appreciable transverse magnetization components, which can be detected experimentally by torque measurements. Such measurements can help to extract a more quantitative estimate of the relevant microscopic couplings.

(2) Fields along **a** [panel (b)] and **c*** [panel (e)] induce a phase transition at a characteristic field strength H_a^* and H_c^*, respectively. Below these fields, the symmetry $\mathcal{M}_{ac^*} \times \mathcal{T}$ is broken spontaneously, and the order parameters of Eq. (52) become nonzero. By contrast, for fields along **b** [panel (h)],

there is no such phase transition, and the mirror symmetry $\mathcal{M}_{ac^*}$ remains intact, irrespective of the field strength.

(3) At the fields H_a^* and H_c^*, the system has almost the same magnetic structure as in zero field but with the total moment turned along the field direction. Here, the applied field works against the effect of $\mathbf{T}_3$ (which favors alignment along the **b** axis, as discussed above) and partly against the in-plane components of the DM vectors (which favor alignment of the total moment in the ac^* plane and predominantly along the **a** axis). Along with the presence of multiple bonds, this can explain the large values obtained for H_a^* and H_c^*.

(4) The combinations of spin components that are driven explicitly by the field (data shown in the last row of panels in Fig. 7) show that (i) the saturation field H_{sat} is beyond 200 T for the microscopic parameters obtained from VASP and (ii) that the way to saturation in panels (c) and (i) involves an abrupt reorientation of the Cu1 spins at some very high fields H_a^{**} and H_b^{**} below H_{sat}. Such a transition is absent for fields along $\mathbf{c}^*$.

(5) According to the results shown in Figs. 7(a), 7(d), and 7(g), the slopes of the longitudinal magnetizations (per Cu) at low fields are $\sim 0.015\,\mu_B/$T for $\mathbf{H} \parallel \mathbf{a}$, $0.008\,\mu_B/$T for $\mathbf{H} \parallel \mathbf{c}^*$, and $0.0015\,\mu_B/$T for $\mathbf{H} \parallel \mathbf{b}$. The corresponding slopes estimated from the experimental data of Zhao *et al.* at 2 K (Fig. 5(b) of Ref. [21]) are 0.015–$0.016\,\mu_B/$T for $\mathbf{H} \parallel \mathbf{a}$, $0.012\,\mu_B/$T for $\mathbf{H} \parallel \mathbf{c}^*$, and $0.0028\,\mu_B/$T for $\mathbf{H} \parallel \mathbf{b}$. The agreement is satisfactory [1].

VIII. IMPACT OF QUANTUM FLUCTUATIONS

The picture presented so far has been entirely classical. The natural next step is to consider the effect of quantum fluctuations and confirm that their impact is minimal in Cu_2OSO_4, as observed experimentally [21,22]. As explained earlier, this aspect cannot be accounted for at the level of the isotropic model description of Cu_2OSO_4, which remains highly frustrated despite the structural peculiarities of this material. The presence of symmetric and antisymmetric exchange anisotropy is crucial for resolving this puzzle as well, as these interactions open an appreciable spin gap (as shown already in Fig. 6), which in turn alleviates the impact of quantum fluctuations. To show this explicitly, we have performed a standard linear spin-wave expansion [49,50] around the ground state of a single layer of Cu_2OSO_4 and for various anisotropic terms included in the Hamiltonian. The multiple-layer problem does not feature any qualitative changes for the in-plane dispersion of the magnons and the on-site spin length reduction.

A. Spin length reduction

Let us take the site labeling convention of Fig. 1 and denote by $\mathbf{w}_j$ ($j = 1$–4) the direction of the four spins of the magnetic unit cell in the classical ground state. Incidentally, recall that these directions are different for $\mathbf{T}_3 = 0$ and for $\mathbf{T}_3 \neq 0$, as the

---

[1] We note that the data reported in Fig. 5(d) of Ref. [21] must correspond to magnetic moment per Cu site and not per formula unit, to be consistent with the main finding of Ref. [21] of a total moment of $1/4\,\mu$B per Cu ion, but also with Ref. [22].
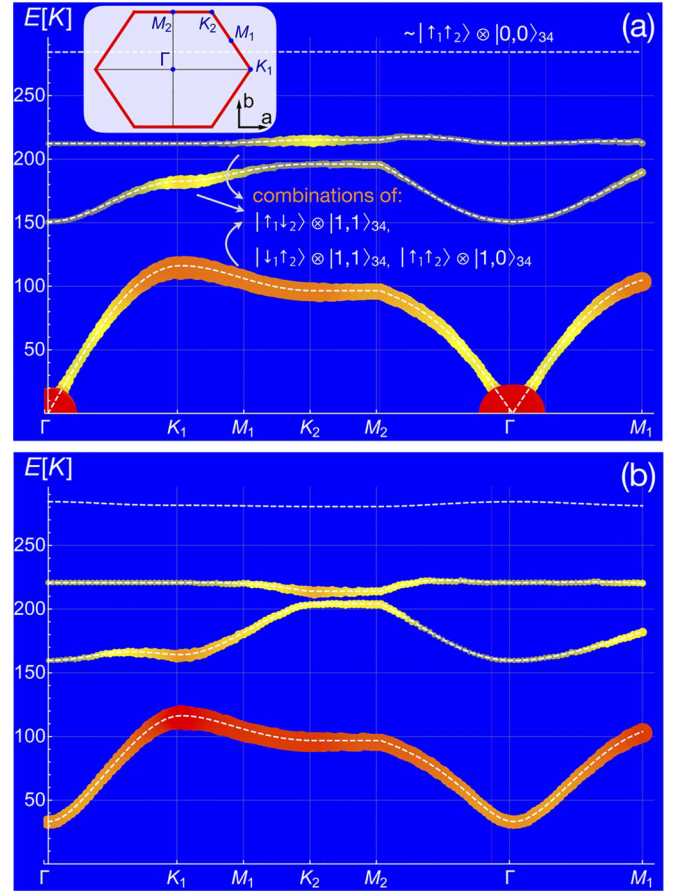

FIG. 8. Linear spin-wave spectra (white dashed lines) and dynamical structure factor intensity $\mathcal{S}(\mathbf{Q}, \omega)$ (symbol size, rescaled to the respective maximum intensity in each separate panel) for a single layer of Cu_2OSO_4, along certain cuts of the Brillouin zone, see inset. In (a), the Hamiltonian includes Heisenberg couplings and the c^* components of the DM couplings, whereas in (b), it includes Heisenberg, all components of the DM vectors, and the interaction matirx $\mathbf{T}_3$.

corresponding ground states are different. The spin length of the jth spin in the renormalized ground state is then given by $\langle S_j^w \rangle = S - \langle n_j \rangle$, where $S = \frac{1}{2}$ and n_j is the number operator for the spin flips (magnons).

For the model without $\mathbf{T}_3$ (and all DM components included), we find

$$\text{DM only}: \begin{cases} \langle S_1^w \rangle = \langle S_2^w \rangle = 0.441, \\ \langle S_3^w \rangle = \langle S_4^w \rangle = 0.456, \end{cases} \quad (54)$$

while for the model with both DM and $\mathbf{T}_3$ included we find

$$\text{DM} + \mathbf{T}_3 : \begin{cases} \langle S_1^w \rangle = \langle S_2^w \rangle = 0.437, \\ \langle S_3^w \rangle = \langle S_4^w \rangle = 0.451. \end{cases} \quad (55)$$

As expected by symmetry, the two Cu2 sites ($j = 3$ and 4) have equal spin length, and the same is true for the two Cu1 sites ($j = 1$ and 2). Moreover, the effect of quantum fluctuations on the Cu2 sites is less severe due to the strong FM J_d exchange. Most importantly, the reduction of the spin length is minimal (at most 12% of the classical length of $\frac{1}{2}$). This is consistent

with experiment [21,22] and corroborates our earlier assertion that the impact of quantum fluctuations in Cu_2OSO_4 is heavily mitigated due to the appreciable anisotropy gap, giving further confidence to the above classical description.

B. Magnon excitations and dynamical structure factor

We will now examine the spin-wave expansion more closely and discuss the magnon excitation spectrum. The uniform states discussed above have a four-site unit cell, and we therefore expect four magnon bands, emerging from the hybridization and delocalization of the four local spin flips on the unit cell.

Figure 8 shows the resulting magnon band structure of a single layer of Cu_2OSO_4. The dispersions shown correspond to special cuts on the ab plane, inside the first BZ, which is an almost symmetric hexagon (see inset). In panel (a), the spin Hamiltonian includes the Heisenberg plus the c^* components of the DM vectors, whereas in panel (b), it includes all DM components as well as the interaction matrix $\mathbf{T}_3$. In panel (a), the lowest mode is gapless at the Γ point because the Hamiltonian with only the c^* components of the DM vectors included has a U(1) symmetry around the $\mathbf{c}^*$ axis, and this symmetry is broken spontaneously by the classical ground state around which we expand. In panel (b), this mode is gapped out due to the in-plane DM components and $\mathbf{T}_3$, as discussed above. Apart from this qualitative difference, the remaining shape and overall positioning of the magnon bands is similar in the two panels, which reflects the fact that the intermediate- and high-energy parts of the excitation spectrum are not affected much by the anisotropies.

On top of the magnon bands of Fig. 8, we also show by symbols (filled circles) the zero-temperature dynamical structure factor intensity (more specifically, its trace):

$$\mathcal{S}(\mathbf{Q}, \omega) = \int \frac{d\omega}{2\pi} \langle \mathbf{M}(\mathbf{Q}, t) \cdot \mathbf{M}(-\mathbf{Q}, 0) \rangle, \quad (56)$$

where $\mathbf{M}(\mathbf{Q}, t)$ is the time-evolved Fourier transform of the magnetization evaluated at wave vector $\mathbf{Q}$ and time t. The size of the symbols (and color) is scaled relative to the maximum intensity in each separate panel. The majority of the scattering weight is carried by the three lowest magnon branches. The fourth magnon band carries almost no weight at all and features a much weaker dispersion with the bandwidth of the order of a few Kelvin.

C. Further analysis of the magnon bands

To gain some understanding of the overall magnon band structure, we proceed to a more in-depth analysis of the magnon modes. To that end, we take again the four-site labeling of the unit cell of Eq. (7) and use, for each separate spin, the local quantization axis pertaining to the direction of that spin in the reference classical state around which we wish to expand. With this choice, the reference state is the tensor product of

$$|\uparrow_1 \uparrow_2\rangle \otimes |S_{34} = 1, M_{34} = 1\rangle, \quad (57)$$

over all unit cells, where S_{34} is the total spin quantum number of the Cu2 dimer and M_{34} is its projection along the local quantization axis. At the mean-field level, the four magnon

states and their corresponding excitation energies ΔE (measured from the reference state) are

$$
\begin{aligned}
&|\uparrow_1 \uparrow_2\rangle \otimes |S_{34} = 1, M_{34} = 0\rangle, \quad &\Delta E = h_3, \\
&|\uparrow_1 \downarrow_2\rangle \otimes |S_{34} = 1, M_{34} = 1\rangle, \quad &\Delta E = h_1, \\
&|\downarrow_1 \uparrow_2\rangle \otimes |S_{34} = 1, M_{34} = 1\rangle, \quad &\Delta E = h_1, \\
&|\uparrow_1 \uparrow_2\rangle \otimes |S_{34} = 0, M_{34} = 0\rangle, \quad &\Delta E = |J_d| + h_3,
\end{aligned}
\quad (58)
$$

where $h_3 = h_4$ is the magnitude of the local mean field exerted on a Cu2 site from its Cu1 neighbors, and similarly, $h_1 = h_2$ is the magnitude of the local mean field exerted on a Cu1 site from all its neighbors. Specifically,

$$
\begin{aligned}
\mathbf{h}_1 &= -2J_3\langle \mathbf{S}_2 \rangle - 2(J_1 + J_2)\langle \mathbf{S}_3 \rangle, \\
\mathbf{h}_3 &= -(J_1 + J_2)(\langle \mathbf{S}_1 \rangle + \langle \mathbf{S}_2 \rangle),
\end{aligned}
\quad (59)
$$

where $\langle \mathbf{S}_j \rangle$ ($j = 1$–4) are the spin vectors in the classical reference state around which we expand. For the isotropic model, the magnitudes of these fields are given by

$$h_1 = J_3, \quad h_3 = \frac{(J_1 + J_2)^2}{2J_3}, \quad (60)$$

whereas in the presence of anisotropies, their values can be obtained numerically.

The first member of Eq. (58) is the symmetric combination of the two single spin flips on the J_d dimer:

$$|S_{34} = 1, M_{34} = 0\rangle = \frac{1}{\sqrt{2}}(|\uparrow_3\downarrow_4\rangle + |\downarrow_3\uparrow_4\rangle), \quad (61)$$

whereas the last member of Eq. (58) is the antisymmetric (singlet) combination:

$$|S = 0, M = 0\rangle_{3,4} = \frac{1}{\sqrt{2}}(|\uparrow_3\downarrow_4\rangle - |\downarrow_3\uparrow_4\rangle). \quad (62)$$

Returning to Fig. 8(a), it turns out the three lowest magnon branches arise, almost entirely, by the hybridization and delocalization of the first three members of Eq. (58), whereas the fourth band, which resides at around $E = 284$ K, is made almost entirely by the fourth member of Eq. (58), i.e., the singlet.

The reason this band is almost flat can be uncovered by examining what happens at the level of the isotropic model, i.e., by disregarding for the moment the effect of DM and $\mathbf{T}_3$ anisotropy. In that model, it can be shown that (i) a singlet excitation on the Cu2 dimer of one unit cell can hop (if $J_1 \neq J_2$) to a Cu2 dimer of a neighboring unit cell only via the intermediate Cu1 sites that connect these dimers; and (ii) due to the geometry of the unit cell, the above hopping to the Cu1 sites is proportional to $J_1 - J_2$. To see this, we simply start from the state $|\uparrow_1 \uparrow_2\rangle \otimes |S_{34} = 0, M_{34} = 0\rangle$ and apply the relevant isotropic interactions J_1 and J_2, which can be grouped in the form:

$$\mathcal{H}_{\text{Cu1-Cu2}} = (\mathbf{S}_1 + \mathbf{S}_2) \cdot (J_1\mathbf{S}_3 + J_2\mathbf{S}_4). \quad (63)$$

One can then show that

$$
\begin{aligned}
\mathcal{H}_{\text{Cu1-Cu2}} &|S_{12} = 1, M_{12} = 1\rangle \otimes |S_{34} = 0, M_{34} = 0\rangle \\
&= \tfrac{1}{2}(J_1 - J_2)\{|S_{12} = 1, M_{12} = 1\rangle \otimes |S_{34} = 1, M_{34} = 0\rangle \\
&\quad - |S_{12} = 1, M_{12} = 0\rangle \otimes |S_{34} = 1, M_{34} = 1\rangle\}. \quad (64)
\end{aligned}
$$

Thus, the hopping of the excitation from the Cu2 dimer to the neighboring Cu1 spins is indeed proportional to $J_1 - J_2$. Now according to the VASP values of Table I, this difference is small (8 K). Thus, the effective hopping from one Cu2 dimer to another is also small, which explains the very weak dispersion of the singlet branch; we have checked explicitly that, for $J_1 = J_2$, the band becomes completely flat, as expected. Additionally, the small hopping amplitude gives a weak hybridization of this band with the remaining three bands, which explains our above statement that this band is made almost entirely of the singlet modes on the Cu2 dimers.

Finally, we note that the $|S_{34} = 1, M_{34} = -1\rangle$ member of the triplet on the Cu2 dimer corresponds, in the language of standard spin-wave expansion, to a two-particle excitation, which is why it does not appear in the spin-wave spectrum of Fig. 8. A generalized, multiboson version of the spin-wave expansion that incorporates the J_d coupling explicitly on the Cu2 bonds reveals this excitation branch in the spectrum around $\Delta E = 2h_3$, which is $\sim$232 K at the level of the model $\mathcal{H}_{\lambda=1}$. The intensity $\mathcal{S}(\mathbf{Q}, \omega)$ of this mode vanishes, as it corresponds to a total $\Delta M = 2$ excitation, relevant to the ground state. However, this mode can be observed, e.g., via magnetic Raman scattering, which would then provide a more direct estimate of $2h_3$ and, in turn, of the microscopic couplings that affect h_3.

IX. SUMMARY AND DISCUSSION

We have presented a comprehensive study of dolerophanite Cu_2OSO_4, a layered kagomelike magnet where every third site of the kagome structure is occupied by a strongly FM spin dimer. We have arrived at a minimal microscopic model that uncovers the origin of most experimental data reported so far [21,22], including the intralayer and interlayer magnetic structure, the reported total magnetic moment, and the observed anisotropy in the direction of the uncompensated moment.

Our results show that the origin of the canted order in Cu_2OSO_4 comes from AFM NN interactions. This fact sets this material apart from francisite and related compounds that feature canted order arising from FM NN interactions frustrated by an AFM coupling between second neighbors [23,51]. In Cu^{2+} compounds, the sign of short-range exchange interactions is usually determined by the Cu–O–Cu angles in the crystal structure. The relevant values for Cu_2OSO_4 are 90.5/104.7° (J_1), 117.6° (J_2), and 114.2° (J_3), all being similar to francisite and closer to 90° than in herbertsmithite ($\sim$119°) with its AFM NN couplings. The AFM nature of J_1, J_2, and J_3 is probably reinforced by the peculiar orbital configuration with the different symmetries of the magnetic orbital on the Cu1 and Cu2 sites, see Fig. 2(d).

Given the AFM couplings in the kagome plane, the canted order can be broadly understood as a deformation of the 120° state expected in KHAFM in the presence of perturbations, such as anisotropy and weak lattice distortions. This order may [52] or may not [53] feature an uncompensated total moment depending on the exact symmetry of the material and the nature of perturbations therein. This canted order in Cu_2OSO_4 is necessarily ferrimagnetic because one out of three sites is occupied by effective spin-1 moments of the Cu2 dimer. An interesting finding of our work is that the θ angle

close to 60° in Cu_2OSO_4, i.e., an almost undistorted 120° configuration, is a combined effect of geometrical frustration and anisotropy. Heisenberg exchange alone should result in much lower values of θ as a result of the sizable deformation of the kagome lattice. However, large anisotropy terms restore $\sim$120° spin configuration that allows a larger energy gain from the out-of-plane DM components.

The large DM anisotropy in Cu_2OSO_4 is quite unusual and striking. It may be traced back to the close competition between $d_{x^2-y^2}$ and $d_{3z^2-r^2}$ as possible magnetic orbitals and the eventual stabilization of different orbitals on different Cu sites. A similar situation is realized in the skyrmion material Cu_2OSeO_3, where the sizable ratio of $|\mathbf{D}/J| \simeq 0.6$ was found for one of the couplings [31]. The simultaneous presence of $d_{x^2-y^2}$ and $d_{3z^2-r^2}$ magnetic orbitals may thus be a promising route for realizing the large DM interaction regime experimentally. At any rate, a complete understanding of the precise mechanism behind the large DM interactions is still lacking and warrants further dedicated investigations, e.g., via superexchange expansions that incorporate the precise low-symmetry crystal field of the two Cu sites, the various hopping amplitudes, and the effect of the spin-orbit coupling.

The presence of strong anisotropy is consistent with the fact that the observed magnetic moment is almost classical [21,22]. This agrees with our linear spin-wave calculations, which demonstrate that the reduction of the spin length is very small in the presence of anisotropy. The latter ingredient is crucial because the isotropic model description of Cu_2OSO_4 delivers an infinite ground-state degeneracy at the classical level, which in turn is expected to give rise to large quantum fluctuations.

Another key result is that the observed direction of the uncompensated moment results from a peculiar competition between the antisymmetric (DM) and the symmetric part of the exchange anisotropy, which gives rise to a two-step reorientation process involving two continuous phase transitions.

One of the remaining open issues is the size of the magnon gap. Previous studies reported a small value of 1.14 K using AFM resonance [20], but the exact nature of the mode probed in this experiment remains to be understood. To facilitate this understanding, we have presented predictions for further experiments, which can allow for a more quantitative refining of the microscopic coupling parameters. These include (i) the behavior of Cu_2OSO_4 under magnetic fields along different crystallographic directions and the corresponding prediction of appreciable transverse magnetization that can be measured by torque experiments, (ii) the prediction of the magnon excitation spectrum (and the associated dynamical spin structure factor) which can be measured by inelastic neutron scattering experiments, and (iii) the prediction for the presence of a flat two-particle mode involving the $|S_{34} = 1, M_{34} = -1\rangle$ member of the triplet on the Cu2 dimers, with excitation energy $\Delta E = 2h_3$, which can be measured by Raman scattering.

We hope these predictions and the minimal model uncovered in this paper will provide the basic framework and necessary guidelines for further theoretical and experimental works in Cu_2OSO_4 and related materials.

TABLE III. Positions of the Cu atoms mentioned in Table I, in fractional units (crystallographic coordinates) and in Å (Cartesian coordinates). In the third row from the end, the notation Cu23 = Cu21p + **a** + **c** means that the displacement vector connecting the atoms labels as Cu23 and Cu21p is **a** + **c**.

Cu site	Fractional units	$\mathbf{r}$ in abc^*-frame (in Å)
Cu21	(0.0721, 0, 0.2182)	(−0.2161, 0, 1.4083)
Cu21p	(−0.0721, 0, −0.2182)	(0.2161, 0, −1.4083)
Cu22	(0.5721, 0.5, 0.2182)	(4.4689, 3.1595, 1.4083)
Cu22p	(0.4279, 0.5, −0.2182)	(4.9011, 3.1595, −1.4083)
Cu23 = Cu21p + **a** + **c**	(0.9279, 0, 0.7818)	(5.4997, 0, 5.0458)
Cu11	(0.25, 0.25, 0)	(2.3425, 1.57975, 0)
Cu14	(0.25, 0.75, 0)	(2.3425, 4.73925, 0)

APPENDIX A: STRUCTURAL ASPECTS

Cu_2OSO_4 crystallizes in a monoclinic crystal system with space group $C2/m$ [17]. The lengths of the primitive translations along the three crystallographic axes are $a = 9.370$ Å, $b = 6.319$ Å, and $c = 7.639$ Å, and the angles between these axes are $\alpha = \gamma = \pi/2$ and $\beta = 122.34°$. Table III shows the actual positions of the Cu atoms mentioned in Table I.

APPENDIX B: CURIE-WEISS TEMPERATURE FOR ANISOTROPIC INTERACTIONS

Here, we provide a general formula for the Curie-Weiss temperature Θ_{CW} in a magnetic system with general anisotropic interactions. To that end, we consider a spin Hamiltonian of the form:

$$\mathcal{H} = \sum_{i<j} \mathbf{S}_i \cdot \mathbf{K}_{ij} \cdot \mathbf{S}_j, \tag{B1}$$

where $\mathbf{K}_{ij}$ is a 3×3 matrix that embodies all possible bilinear couplings between spins at sites i and j. This coupling can be decomposed into the Heisenberg exchange J_{ij}, the DM anisotropy described by the DM vector $\mathbf{D}_{ij}$, and the symmetric and traceless part $\mathbf{T}_{ij}$ of $\mathbf{K}_{ij}$, as follows:

$$\mathbf{K}_{ij} = J_{ij}\mathbf{1} + \mathbf{A}_{ij} + \mathbf{T}_{ij}, \tag{B2}$$

where $\mathbf{1}$ is the 3×3 identity matrix,

$$J_{ij} = \tfrac{1}{3}\text{Tr}(\mathbf{K}_{ij}), \tag{B3}$$

$$\mathbf{A}_{ij} = \tfrac{1}{2}(\mathbf{K}_{ij} - \mathbf{K}_{ji}), \quad D_{ij}^\alpha = \epsilon^{\alpha\beta\gamma}\mathbf{A}_{ij}^{\beta\gamma}, \tag{B4}$$

$$\mathbf{T}_{ij} = \tfrac{1}{2}(\mathbf{K}_{ij} + \mathbf{K}_{ji}) - J_{ij}\mathbf{1}, \quad \text{Tr}(\mathbf{T}_{ij}) = 0, \tag{B5}$$

where $\epsilon^{\alpha\beta\gamma}$ is the Levi-Civita symbol, and α, β, and γ are Cartesian components.

Next, we would like to perform a high-T expansion of the magnetic susceptibility and extract a formula for Θ_{CW} which, in general, will depend on the direction of the applied magnetic field $\mathbf{H}$. To that end, we use a mean-field decoupling, which is generally valid at high enough temperatures where the correlation length is very small. Due to the magnetic anisotropy, the direction of the (thermal averaged) field-induced moments $\langle\mathbf{S}_i\rangle$ are not necessarily the same. The total field exerted at site i, including the external field, is given by

$$\mathbf{h}_i = -\frac{1}{g\mu_B}\sum_j \mathbf{K}_{ij} \cdot \langle\mathbf{S}_j\rangle + \mathbf{H}, \tag{B6}$$

where the minus sign in the first term on the right-hand side follows from our convention for the Zeeman energy of site i, which is $-g\mu_B\mathbf{S}_i \cdot \mathbf{H}$. For spin-$\frac{1}{2}$, the thermal average $\langle\mathbf{S}_i\rangle$ in the mean-field decoupled problem, at temperature T, equals

$$\langle\mathbf{S}_i\rangle = \frac{1}{2}\tanh\left(\frac{g\mu_B h_i}{2k_B T}\right)\hat{\mathbf{h}}_i, \tag{B7}$$

where $h_i = |\mathbf{h}_i|$ is the magnitude of the local field and $\hat{\mathbf{h}}_i$ is its direction. In the high-T limit, we can replace

$$\langle\mathbf{S}_i\rangle = \frac{g\mu_B}{4k_B T}\mathbf{h}_i. \tag{B8}$$

Using Eq. (B7) then gives

$$\langle S_i^\mu\rangle + r\sum_{j\nu} K_{ij}^{\mu\nu}\langle S_j^\nu\rangle = rg\mu_B H^\mu, \tag{B9}$$

where we have defined $r \equiv 1/(4k_B T)$. We note in passing that, for general spin S, this expression must be replaced with $r = S(S+1)/(3k_B T)$. With varying i and μ, Eq. (B9) is a system of coupled equations which can be written in the compact form:

$$\mathbf{\Lambda} \cdot \boldsymbol{\sigma} = \mathbf{f}, \tag{B10}$$

where, using the abc^* frame,

$$\boldsymbol{\sigma} = \begin{pmatrix} \langle S_1^a\rangle \\ \langle S_1^b\rangle \\ \langle S_1^{c^*}\rangle \\ \langle S_2^a\rangle \\ \vdots \\ \langle S_N^{c^*}\rangle \end{pmatrix}, \quad \mathbf{f} = rg\mu_B\begin{pmatrix} H^a \\ H^b \\ H^{c^*} \\ H^a \\ \vdots \\ H^{c^*} \end{pmatrix}, \tag{B11}$$

and $\Lambda_{i\mu,j\nu} = \delta_{ij}\delta_{\mu\nu} + rK_{ij}^{\mu\nu}$, or more compactly, $\mathbf{\Lambda} = \mathbf{1} + r\mathbf{K}$. The solution of Eq. (B10) can be expanded in powers of r (or equivalently, in powers of $1/T$):

$$\boldsymbol{\sigma} = \mathbf{\Lambda}^{-1} \cdot \boldsymbol{f} = (\mathbf{1} + r\mathbf{K})^{-1} \cdot \boldsymbol{f} = (\mathbf{1} - r\mathbf{K}) \cdot \boldsymbol{f} + O(r^3). \quad \text{(B12)}$$

That is,

$$\langle S_i^\mu \rangle = r\, g\mu_B \sum_\mu \left(\delta_{\mu\nu} - r \sum_j K_{ij}^{\mu\nu} \right) H^\nu + O(r^3). \quad \text{(B13)}$$

Suppose now that we wish to obtain the diagonal elements of the susceptibility tensor. We apply the field in a fixed direction, say μ, and calculate the total spin (per site) along the same direction:

$$\frac{\langle S_{\text{tot}}^\mu \rangle}{N} = g\mu_B \left(r - r^2 \sum_{ij} \frac{K_{ij}^{\mu\mu}}{N} \right) H + O(r^3), \quad \text{(B14)}$$

from which we can read off the Curie-Weiss temperature by comparing with the high-T expansion of the Curie-Weiss law:

$$\chi_{\mu\mu} = \frac{C}{T - \Theta_{\text{CW}}^{\mu\mu}} = \frac{C}{T} + \frac{C\Theta_{\text{CW}}^{\mu\mu}}{T^2} + O\left(\frac{1}{T^3} \right). \quad \text{(B15)}$$

We find, for general S,

$$k_B\Theta_{\text{CW}}^{\mu\mu} = -\frac{S(S+1)}{3} \frac{1}{N} \sum_{ij} K_{ij}^{\mu\mu}$$

$$= -\frac{S(S+1)}{3} \frac{2}{N} \sum_{i<j} \left(J_{ij} + T_{ij}^{\mu\mu} \right), \quad \text{(B16)}$$

where in the second step, we used Eq. (B2). Note that the DM interactions do not contribute to the Curie-Weiss temperature because of the antisymmetry of the tensor $\mathbf{A}_{ij}$.

Applying Eq. (B16) to the full model that we consider in the main text (which includes Heisenberg exchange, DM vectors, and the symmetric anisotropy $\mathbf{T}_3$) gives

$$\Theta_{\text{CW}}^{aa} = -\tfrac{1}{8}\big[J_d + 2(J_3 + J_{\perp,2}) + 4(J_1 + J_2 + J_\perp) + 2T_3^{aa} \big],$$

$$\Theta_{\text{CW}}^{bb} = -\tfrac{1}{8}\big[J_d + 2(J_3 + J_{\perp,2}) + 4(J_1 + J_2 + J_\perp) + 2T_3^{bb} \big],$$

$$\Theta_{\text{CW}}^{c^*c^*} = -\tfrac{1}{8}\big[J_d + 2(J_3 + J_{\perp,2}) + 4(J_1 + J_2 + J_\perp) + 2T_3^{c^*c^*} \big],$$

$$\text{(B17)}$$

which reduces to Eq. (6) in the absence of $\mathbf{T}_3$.

[1] *Frustrated Spin Systems*, 2nd ed. (World Scientific, Singapore, 2013)

[2] C. Lacroix, P. Mendels, and F. Mila (Eds.), *Introduction to Frustrated Magnetism: Materials, Experiments, Theory (Springer Series in Solid-State Sciences)*, 2011th ed. (Springer, Berlin, 2011).

[3] A. P. Ramirez, Strongly geometrically frustrated magnets, Annu. Rev. Mater. Sci. **24**, 453 (1994).

[4] J. Richter, J. Schulenburg, and A. Honecker, Quantum magnetism in two dimensions: From semi-classical Néel order to magnetic disorder, in *Quantum Magnetism*, edited by U. Schollwöck, J. Richter, D. J. J. Farnell, and R. F. Bishop (Springer, Berlin, 2004), pp. 85–153.

[5] P. A. Lee, An end to the drought of quantum spin liquids, Science **321**, 1306 (2008).

[6] L. Balents, Spin liquids in frustrated magnets, Nature (London) **464**, 199 (2010).

[7] M. R. Norman, Colloquium: Herbertsmithite and the search for the quantum spin liquid, Rev. Mod. Phys. **88**, 041002 (2016).

[8] L. Savary and L. Balents, Quantum spin liquids: a review, Rep. Prog. Phys. **80**, 016502 (2017).

[9] Y. Zhou, K. Kanoda, and T.-K. Ng, Quantum spin liquid states, Rev. Mod. Phys. **89**, 025003 (2017).

[10] P. Anderson, Resonating valence bonds: A new kind of insulator? Mater. Res. Bull. **8**, 153 (1973).

[11] P. Fazekas and P. W. Anderson, On the ground state properties of the anisotropic triangular antiferromagnet, Philos. Mag. **30**, 423 (1974).

[12] P. W. Anderson, The resonating valence bond state in La$_2$CuO$_4$ and superconductivity, Science **235**, 1196 (1987).

[13] S. Liang, B. Doucot, and P. W. Anderson, Some new variational resonating-valence-bond-type wave functions for the spin-$\frac{1}{2}$ an-tiferromagnetic Heisenberg model on a square lattice, Phys. Rev. Lett. **61**, 365 (1988).

[14] M. J. P. Gingras and P. A. McClarty, Quantum spin ice: A search for gapless quantum spin liquids in pyrochlore magnets, Rep. Prog. Phys. **77**, 056501 (2014).

[15] P. Mendels and F. Bert, Quantum kagome frustrated antiferromagnets: One route to quantum spin liquids, C. R. Phys. **17**, 455 (2016).

[16] E. Flügel-Kahler, Die Kristallstruktur von Dolerophanit, Cu$_2$O(SO$_4$), Acta Cryst. **16**, 1009 (1963).

[17] H. Effenberger, Cu$_2$O(SO$_4$), dolerophanite: Refinement of the crystal structure, with a comparison of [OCu(II)$_4$] tetrahedra in inorganic compounds, Chem. Mon. **116**, 927 (1985).

[18] A. R. Ginting, B. H. O'Connor, and J. G. Dunn, X-ray powder data for synthetic dolerophanite, copper(II) oxysulphate [Cu$_2$O(SO$_4$)], Powder Diffr. **9**, 21 (1994).

[19] W. Martens, R. L. Frost, J. T. Kloprogge, and P. A. Williams, Raman spectroscopic study of the basic copper sulphates—Implications for copper corrosion and 'bronze disease', J. Raman Spectrosc. **34**, 145 (2003).

[20] N. Takahashi, S. Okubo, H. Ohta, T. Sakurai, M. Fujisawa, and H. Kikuchi, Dzyaloshinsky-Moriya interaction estimated by AFMR of kagome like substance Cu$_2$OSO$_4$ observed at 1.8 K, J. Phys.: Conf. Ser. **400**, 032097 (2012).

[21] L. Zhao, C. Dalton, S.-C. Liao, Z. Hu, H.-J. Lin, C.-T. Chen, and A. C. Komarek, Single crystal growth and physical properties of dolerophanite single crystals, Phys. Rev. Mater. **3**, 124403 (2019).

[22] V. Y. Favre, G. S. Tucker, C. Ritter, R. Sibille, P. Manuel, M. D. Frontzek, M. Kriener, L. Yang, H. Berger, A. Magrez *et al.*, Ferrimagnetic 120° magnetic structure in Cu$_2$OSO$_4$, Phys. Rev. B **102**, 094422 (2020).

[23] I. Rousochatzakis, J. Richter, R. Zinke, and A. A. Tsirlin, Frustration and Dzyaloshinsky-Moriya anisotropy in the kagome francisites $Cu_3Bi(SeO_3)_2O_2X$ (X = Br, Cl), Phys. Rev. B **91**, 024416 (2015).

[24] I. Dzyaloshinsky, A thermodynamic theory of "weak" ferromagnetism of antiferromagnetics, J. Phys. Chem. Solids **4**, 241 (1958).

[25] T. Moriya, New mechanism of anisotropic superexchange interaction, Phys. Rev. Lett. **4**, 228 (1960).

[26] K. Koepernik and H. Eschrig, Full-potential nonorthogonal local-orbital minimum-basis band-structure scheme, Phys. Rev. B **59**, 1743 (1999).

[27] G. Kresse and J. Furthmüller, Efficiency of *ab-initio* total energy calculations for metals and semiconductors using a plane-wave basis set, Comput. Mater. Sci. **6**, 15 (1996).

[28] G. Kresse and J. Furthmüller, Efficient iterative schemes for *ab initio* total-energy calculations using a plane-wave basis set, Phys. Rev. B **54**, 11169 (1996).

[29] J. P. Perdew, K. Burke, and M. Ernzerhof, Generalized gradient approximation made simple, Phys. Rev. Lett. **77**, 3865 (1996).

[30] V. V. Mazurenko, M. V. Valentyuk, R. Stern, and A. A. Tsirlin, Nonfrustrated interlayer order and its relevance to the Bose-Einstein condensation of magnons in $BaCuSi_2O_6$, Phys. Rev. Lett. **112**, 107202 (2014).

[31] O. Janson, I. Rousochatzakis, A. A. Tsirlin, M. Belesi, A. A. Leonov, U. K. Rößler, J. van den Brink, and H. Rosner, The quantum nature of skyrmions and half-skyrmions in Cu_2OSeO_3, Nat. Commun. **5**, 5376 (2014).

[32] A. A. Tsirlin, O. Janson, and H. Rosner, β-$Cu_2V_2O_7$: A spin-$\frac{1}{2}$ honeycomb lattice system, Phys. Rev. B **82**, 144416 (2010).

[33] H. J. Xiang, E. J. Kan, S.-H. Wei, M.-H. Whangbo, and X. G. Gong, Predicting the spin-lattice order of frustrated systems from first principles, Phys. Rev. B **84**, 224429 (2011).

[34] A. A. Tsirlin, Spin-chain magnetism and uniform Dzyaloshinsky-Moriya anisotropy in BaV_3O_8, Phys. Rev. B **89**, 014405 (2014).

[35] A. A. Tsirlin, *Ab initio* results for dolerophanite, Cu_2OSO_4, http://doi.org/10.5281/zenodo.8219317.

[36] O. Janson, J. Richter, P. Sindzingre, and H. Rosner, Coupled frustrated quantum spin-$\frac{1}{2}$ chains with orbital order in volborthite $Cu_3V_2O_7(OH)_2 \cdot 2H_2O$, Phys. Rev. B **82**, 104434 (2010).

[37] H. Yoshida, J. Yamaura, M. Isobe, Y. Okamoto, G. J. Nilsen, and Z. Hiroi, Orbital switching in a frustrated magnet, Nat. Commun. **3**, 860 (2012).

[38] V. Elser, Nuclear antiferromagnetism in a registered ^{3}He solid, Phys. Rev. Lett. **62**, 2405 (1989).

[39] A. B. Harris, C. Kallin, and A. J. Berlinsky, Possible Néel orderings of the kagomé antiferromagnet, Phys. Rev. B **45**, 2899 (1992).

[40] D. A. Huse and A. D. Rutenberg, Classical antiferromagnets on the kagomé lattice, Phys. Rev. B **45**, 7536 (1992).

[41] J. T. Chalker and J. F. G. Eastmond, Ground-state disorder in the spin-$\frac{1}{2}$ kagomé Heisenberg antiferromagnet, Phys. Rev. B **46**, 14201 (1992).

[42] D. Lyons and T. Kaplan, A cluster method for finding minimum energy spin states, J. Phys. Chem. Solids **25**, 645 (1964).

[43] A. Chubukov, Order from disorder in a kagomé antiferromagnet, Phys. Rev. Lett. **69**, 832 (1992).

[44] O. Götze, D. J. J. Farnell, R. F. Bishop, P. H. Y. Li, and J. Richter, Heisenberg antiferromagnet on the kagome lattice with arbitrary spin: A higher-order coupled cluster treatment, Phys. Rev. B **84**, 224428 (2011).

[45] A. L. Chernyshev and M. E. Zhitomirsky, Quantum selection of order in an *XXZ* antiferromagnet on a kagome lattice, Phys. Rev. Lett. **113**, 237202 (2014).

[46] A. Ralko, F. Mila, and I. Rousochatzakis, Microscopic theory of the nearest-neighbor valence bond sector of the spin-$\frac{1}{2}$ kagome antiferromagnet, Phys. Rev. B **97**, 104401 (2018).

[47] V. V. Mazurenko, S. L. Skornyakov, V. I. Anisimov, and F. Mila, First-principles investigation of symmetric and antisymmetric exchange interactions of $SrCu_2(BO_3)_2$, Phys. Rev. B **78**, 195110 (2008).

[48] V. V. Mazurenko, S. L. Skornyakov, A. V. Kozhevnikov, F. Mila, and V. I. Anisimov, Wannier functions and exchange integrals: The example of $LiCu_2O_2$, Phys. Rev. B **75**, 224408 (2007).

[49] J.-P. Blaizot and G. Ripka, *Quantum Theory of Finite Systems* (MIT Press, Cambridge, 1986), Chap. 3.

[50] R. M. White, *Quantum Theory of Magnetism*, 3rd ed. (Springer-Verlag, Berlin, 2007).

[51] E. Constable, S. Raymond, S. Petit, E. Ressouche, F. Bourdarot, J. Debray, M. Josse, O. Fabelo, H. Berger, S. deBrion *et al.*, Magnetic and dielectric order in the kagomelike francisite $Cu_3Bi(SeO_3)_2O_2Cl$, Phys. Rev. B **96**, 014413 (2017).

[52] R. Okuma, T. Yajima, D. Nishio-Hamane, T. Okubo, and Z. Hiroi, Weak ferromagnetic order breaking the threefold rotational symmetry of the underlying kagome lattice in $CdCu_3(OH)_6(NO_3)_2 \cdot H_2O$, Phys. Rev. B **95**, 094427 (2017).

[53] K. Iida, H. K. Yoshida, A. Nakao, H. O. Jeschke, Y. Iqbal, K. Nakajima, S. Ohira-Kawamura, K. Munakata, Y. Inamura, N. Murai *et al.*, $q = 0$ long-range magnetic order in centennialite $CaCu_3(OD)_6Cl_2 \cdot 0.6D_2O$: A spin-$\frac{1}{2}$ perfect kagome antiferromagnet with $J_1 - J_2 - J_d$, Phys. Rev. B **101**, 220408(R) (2020).